Comparison and Dynamic interaction between Auditory Cortex and Prefrontal Cortex of Behaving Monkeys during Novelty Detection

Haoxuan Xu[1,2,3,4,9], Peirun Song[1,3,9], Hangting Ye[1,3,9], Qichen Zhang[1], Yuying Zhai[1,3], Xuhui Bao[4], Ishrat Mehmood[4], Hisashi Tanigawa[4], Zhiyi Tu[2], Lingling Zhang[2], Xuan Zhao[2], David Pérez-González[5,6,7], Manuel S. Malmierca[5,6,8] and Xiongjie Yu[1,2,3,4,10*]*

[1] Department of Anesthesia, Women's Hospital, Zhejiang University School of Medicine, Hangzhou, Zhejiang Province, China

[2] Department of Anesthesiology, Shanghai Tenth People's Hospital, Tongji University School of Medicine, Shanghai, China

[3] Zhejiang Provincial Key Laboratory of Precision Diagnosis and Therapy for Major Gynecological Diseases, Women's Hospital, Zhejiang University School of Medicine, Hangzhou, Zhejiang, China

[4] College of Biomedical Engineering and Instrument Science, Zhejiang University, Hangzhou, China

[5] Cognitive and Auditory Neuroscience Laboratory (Lab 1), Institute of Neuroscience of Castilla y León (INCYL), University of Salamanca, Salamanca, Spain

[6] Institute for Biomedical Research of Salamanca (IBSAL), Spain

[7] Department of Basic Psychology, Psychobiology and Methodology of Behavioral Sciences, Faculty of Psychology, University of Salamanca, Spain

[8] Department of Cell Biology and Pathology, Faculty of Medicine, University of Salamanca, Spain

[9] These authors contributed equally

[10] Lead contact: Xiongjie Yu (yuxiongj@gmail.com)

[*] Corresponding authors: yuxiongj@gmail.com (X.Y.), msm@usal.es (M.S.M)

Key Words: Predictive Coding Theory; Macaque Monkey; Oddball Paradigm; Auditory Cortex; Prefrontal Cortex

Acknowledgments

We are grateful to Xiaokai Kou for his help with the experiments. This work was supported by STI2030-Major Projects (2022ZD0204600 and 2022ZD0204800) to XY; National Natural Science Foundation of China (32171044 to XY and 32100827 to YZ), the European Union's Horizon 2020 research and innovation programme under grant agreement No 952378 and Foundation Ramón Areces to MSM and DPG and the Spanish Agencia Estatal de Investigación [(AEI), PID2019-104570RB-I00] to MSM.

Author contributions

Conceptualization, X.Y.; Methodology, X.Y., H.X. and P.S.; Investigation and Data Curation, H.X., P.S., H.Y., Q.Z., X.D. and Y.Z.; Writing-Original Draft, X.Y., H.X., P.S., D.P.G. and M.S.M; Writing-Review & Editing, H.X., P.S., X.Y., D.P.G. and M.S.M; Funding Acquisition, X.Y., Y.Z. and M.S.M; Resources, H.T. and X.Y.; Software, H.X., P.S., H.Y., X.B., Y.Z., I.M., Z.T., L.Z. and X.Z.; Validation and Visualization, H.X. and P.S.; Supervision, X.Y.

Declaration of interests

The authors declare no competing interests.

Abstract

The ability to detect deviations from expected sensory input is critical for adaptive behavior. Here, we investigated the neural dynamics of novelty detection in the auditory cortex (AC) and prefrontal cortex (PFC) of macaques performing an auditory oddball task. Using high-density electrocorticography and Granger causality analyses (GCA), we identified distinct repetition-related signals in both regions: the AC showed both suppression and facilitation to repeated stimuli, while the PFC exhibited robust enhancement, particularly in low-frequency (2 Hz) oscillatory activity. These predictive responses were accompanied by bidirectional AC-PFC coupling in the delta band, reflecting a temporally coordinated predictive state. Deviant tones elicited early responses in the AC, followed by PFC activation, and were associated with increased feedforward and feedback connectivity across delta, theta, and gamma bands. Task engagement amplified both prediction and prediction-error signals, enhancing interareal interactions and behavioral selectivity. Our results reveal that the AC encodes early sensory regularities and violations, while the PFC supports integrative and state-dependent prediction, jointly forming a distributed cortical network for hierarchical predictive coding.

Introduction

Organisms constantly encounter a multitude of stimuli, yet only a fraction are truly significant, with the majority being routine or inconsequential and thus ignored. The ability to detect novel information is therefore vital, allowing adaptive behavioral modifications that enhance survival and reproductive success. Sensory input salience is shaped by environmental context, resulting in behavioral responses that vary based on prior experiences [1-5]. The auditory system, in particular, employs efficient filtering mechanisms to simplify complex acoustic signals into manageable forms [6-8]. At the auditory nerve, initial robust responses to stimuli diminish over milliseconds, stabilizing at a steady-state rate—a process termed spike-frequency adaptation, which prevents overstimulation of higher processing centers [9,10]. Without such mechanisms, indiscriminate neural responses would overwhelm cognitive capacities. To mitigate this, certain auditory neurons exhibit stimulus-specific adaptation (SSA), reducing activity in response to repetitive sounds while remaining responsive to novel stimuli [11-20]. On the macroscopic level, mismatch negativity (MMN)—an event-related potential observed in human electroencephalogram (EEG) studies—has been suggested to be related with novelty detection [21-23]. SSA and MMN optimize auditory processing by selectively representing changes in the auditory scene, ensuring efficiency and adaptability.

SSA or MMN have been extensively investigated using the classical oddball paradigm in animal models, with their presence documented across diverse brain regions, including the auditory midbrain and cortex, and across species and arousal

states [11,12,15,24-26]. Despite these advances, most SSA and MMN studies have relied on sounds lacking behavioral relevance, leaving critical gaps in understanding the influence of prior experiences and SSA (MMN)'s role as an indicator of neuronal plasticity [8,18,24,27-29]. Furthermore, many of these findings were obtained from subjects not engaged in cognitive behavioral tasks, underscoring the need for research into the behavioral context of SSA and MMN [18,24,30,31]. Non-human primates, given their similarity to humans in brain structure and function, provide a valuable model for studying novelty detection behaviorally [32-34]. They exhibit auditory capabilities akin to humans, such as speech discrimination, sound localization, and responses to surprising sounds, making macaques particularly well-suited for investigating the mechanisms underlying novelty detection.

SSA and MMN are integral to predictive coding frameworks, with prediction errors appearing to intensify along the auditory pathway—from the inferior colliculus (IC) to the auditory cortex (AC), and within the AC from primary to higher-order regions [35-38]. While these findings shed light on the hierarchical processing of novelty detection, they offer limited insight into interregional interactions, particularly concerning prediction and prediction error functions. It has been proposed that predictions and prediction errors operate in distinct frequency bands—lower frequencies for predictions and higher frequencies for prediction errors—and are generated in higher and lower brain regions [39-42], respectively. However, experimental evidence supporting this is scarce. To investigate these hypotheses, simultaneous recordings from both higher and lower brain areas are necessary. The AC and prefrontal

cortex (PFC) are suitable candidates, as both are implicated in novelty detection [40,43-46]. The comparative roles of the AC and PFC in prediction and prediction error, during novelty detection remain poorly understood, particularly regarding their interactions during these cognitive processes. These functions are vital for adaptive behavior, enabling organisms to anticipate future events, recognize discrepancies between expectations and reality, and make informed decisions based on sensory input. Analyzing the interactions between the AC and PFC, especially through directional influences measured by Granger causality [47-49], could elucidate the neural circuitry underlying these functions. Understanding the neural mechanisms of novelty detection in behaving non-human primates, focusing on the comparative and interactive roles of the AC and PFC in prediction and predictive error is essential for advancing our knowledge of cognitive processing.

In this study, we address these gaps by investigating the neural mechanisms underlying novelty detection in the AC and PFC of behaving macaques. Using a behaviorally relevant auditory oddball task and simultaneous electrocorticographic recordings from both regions, we examined how predictive processing and prediction error signals are represented and interact across the cortical hierarchy. By applying Granger causality analyses, we assessed the directionality and frequency-specific characteristics of interareal communication. Our results reveal distinct repetition-dependent dynamics in AC and PFC, enhanced low-frequency coupling during auditory regularity, and temporally structured prediction error signaling following deviant stimuli. Crucially, these processes were strongly modulated by task

engagement, indicating that behavioral relevance amplifies both prediction and prediction error representations. Together, these findings elucidate how AC and PFC jointly support predictive coding in a context-dependent manner and advance our understanding of the cortical computations that enable flexible auditory perception.

Results

Prediction during novelty detection in AC and PFC

To dissect neural and behavioral mechanisms underlying novelty detection, two macaques performed a novelty detection task based on an auditory oddball paradigm comprising sequential tone blocks (7–10 repetitions/block). Each block concluded with either a standard tone (identical to preceding tones) or a frequency-deviant tone (Figs. 1A). Monkeys were trained to press a button within 600 ms following deviant tones (hit trials) and to withhold responses to standards (correct rejections). Behavioral performance scaled with the magnitude of frequency deviation, as shown in a representative session (Fig. 1B). Neural activity was recorded via two 64-channel electrocorticography (ECoG) arrays implanted over the auditory cortex (AC) and prefrontal cortex (PFC), respectively (Fig. 1C). Electrode coverage and anatomical landmarks, including the superior temporal sulcus (STS) and lateral sulcus (LS), are illustrated in Supplementary Figure 1.

We first analyzed neural responses to repeated standard tones. Two distinct response profiles were identified. In the first, exemplified by an AC site, strong responses to the initial tone in a block gradually attenuated across subsequent repetitions (Fig. 2A, top row). Unlike previous reports where suppression typically plateaued by the third repetition [4,5], this site showed sustained attenuation through the tenth tone. This prolonged suppression aligns with predictive suppression, reflecting reduced neural responses under heightened certainty of repeated input [50]. Response attenuation was also evident in the time-frequency domain, with decreased power near

~10 Hz and ~2 Hz (Fig. 2A, bottom row). In contrast, the second response type showed a progressive increase in amplitude from the third to tenth repetition (Fig. 2B, top row), accompanied by enhanced ~2 Hz oscillatory activity at the same AC site (Fig. 2B, bottom row), aligned with the stimulus rhythm. This enhancement is consistent with predictive facilitation, potentially reflecting the buildup of temporal expectations or short-term memory of the auditory sequence [37]. Meanwhile, the example PFC site displayed weak responses to presentations 3-6 but robust activation during repetitions 8-10 (Fig. 2C, top row), paralleled by rising ~2 Hz power in the spectrogram (Fig. 2C, bottom row).

To further characterize repetition-related response dynamics, we aligned neural activity by presentation order. In the example AC site, evoked responses progressively decreased near 100 ms following stimulus onset (Fig. 2D, top panel). In contrast, a second AC site (Fig. 2D, middle panel) and a PFC site (Fig. 2D, bottom panel) exhibited increasing activity centered around 250 ms. These divergent patterns highlight that response amplitude varied systematically with repetition order—decreasing in one AC site and increasing in the other, while the PFC site demonstrated monotonic enhancement across repetitions. These trends were also evident in the corresponding time–frequency representations, particularly within the ~2 Hz band (bottom rows in Fig. 2A–C).

To quantify these effects, we analyzed spectral dynamics by tracking power in the 1.8-2.2 Hz band, centered on the 2 Hz stimulation rhythm corresponding to the 500-ms inter-stimulus interval (ISI) (Fig. 2E). Linear fits (dashed lines in Fig. 2E)

from the 5th to the 9th tone revealed a negative slope for the first example AC site, consistent with predictive suppression, and positive slopes for both the second AC site and the PFC site, indicative of predictive facilitation. At the population level, 57% of AC sites and 76% of PFC sites showed increasing 2-Hz power over repetitions (Fig. 2F). On average, the slope of 2-Hz power was significantly steeper in PFC than in AC ($F(1, 254) = 14.22$, $p < 0.001$, $\eta^2 = 0.05$, two-way ANOVA), suggesting stronger low-frequency entrainment with repetition in the PFC. Together, these findings suggest that predictive facilitation is more pronounced in the PFC, particularly in the temporal dynamics of low-frequency neural activity.

After characterizing the responses to standard stimuli in AC and PFC independently, we examined interregional interactions during the repetition period using Granger causality (GC) analysis. We focused on the 1-3 s interval within each standard tone block, corresponding to the third through seventh tones, and averaged signals across all 64 electrodes per region (Fig. 3A). In the AC→PFC direction, GC spectra exhibited a prominent peak near 2 Hz (Fig. 3A, left panel). A similar peak around 2 Hz was observed in the PFC→AC direction (Fig. 3A, right panel), indicating bidirectional coupling aligned with the stimulus rhythm.

To evaluate frequency-specific interactions, we computed GC across canonical bands: 2 Hz, delta (0.6-4 Hz), theta (4-8 Hz), alpha (8–-14 Hz), beta (14-30 Hz), and gamma (30-70 Hz) (Fig. 3B). In both AC→PFC and PFC→AC directions, GC was strongest at 2 Hz and in the delta band, with minimal connectivity in higher frequencies. To quantify connectivity dynamics, we calculated Spearman correlation

coefficients over time (2-3 s window) for each recording site. For each site, we averaged its GC values with the opposite region and computed temporal correlations. Significant and reliable correlations emerged only in the 2 Hz and delta bands (Fig. 3C), indicating stable, low-frequency interactions during auditory repetition. These findings were consistent across animals, as confirmed in a second monkey (Supplementary Fig. 3). Notably, even when the stimulus repetition rate was increased to 2.5 Hz, GC still peaked near 2 Hz rather than shifting upward (Supplementary Fig. 4A), suggesting that delta-band coupling reflects an intrinsic resonance within the AC-PFC circuit rather than mere entrainment to stimulus timing.

Prediction Error during novelty detection in AC and PFC

Next, we examined neural responses to deviant tones in both AC and PFC. An example AC site displayed robust responses to deviants, with response magnitude scaling according to the frequency deviation from standards (Fig. 4A). In contrast, a representative PFC site showed weak responses to standard tones but pronounced activation in response to deviants (Fig. 4B). To quantify these response dynamics, we employed two metrics: (1) the *first significant time*, defined as the earliest time bin in the cluster-based permutation test showing a statistically significant difference among deviant and standard responses, and (2) the *maximum F-value* across time bins before 350 ms, reflecting prediction-error strength. In the illustrated AC site (Fig. 4A), the first significant time and maximum *F*-value were 38 ms and 20.93, respectively; for the example PFC site (Fig. 4B), these values were 144 ms and 14.27.

At the population level, differences between deviant and standard responses

emerged consistently earlier in AC than in PFC for both monkeys (Fig. 4C; monkey X: $Z = 7.67$, $p < 0.001$, $r = 0.68$; monkey C: $Z = 2.32$, $p = 0.02$, $r = 0.29$, two-tailed Mann-Whitney U test, AC vs. PFC). However, the maximum F-values did not significantly differ between the two regions (Fig. 4D; monkey X: $Z = 1.48$, $p = 0.14$, $r = 0.13$; monkey C: $Z = 0.68$, $p = 0.49$, $r = 0.09$, two-tailed Mann-Whitney U test). Sorting channels according to their first significant times further confirmed the earlier deviance detection in AC (Supplementary Figs. 5A, B). Spatial distributions of the maximum F-values indicated heterogeneity within both AC and PFC, suggesting a potential tonotopic organization of prediction-error signaling (Supplementary Figs. 5C, D).

To assess functional connectivity during deviant processing, we performed Granger causality analysis. Time-frequency GC spectra (aligned to stimulus onset and averaged across channels in monkey X) revealed minimal directional interaction under standard conditions, but a pronounced increase in GC magnitude during deviant trials (1.08 frequency ratio; Fig. 5A). These deviant-induced GC increases appeared within 100 ms, primarily in the delta/theta bands (0.6-8 Hz, AC→PFC), and shifted to theta/alpha frequencies (4-14 Hz, PFC→AC) around 200-300 ms post-stimulus (Fig. 5A, bottom), highlighting dynamic and frequency-specific recruitment of the AC-PFC network for prediction-error signaling.

Topographic GC maps in monkey X further illustrated these effects (Fig. 5B): bidirectional GC between AC and PFC was weak for standards (Fig. 5B, top) but substantially increased for deviants, especially in the AC→PFC direction (Fig. 5B,

middle), with subtraction maps confirming the greatest differences along this pathway (Fig. 5B, bottom). When analyzed across different frequency bands, significant information flow was observed from delta to gamma bands in both directions and in both monkeys (Supplementary Fig. 6). To further examine the temporal dynamics, we calculated correlation matrices of GC values across 64 channels and temporal bins at various frequency ratio pairs (1.04 vs. 1.06, 1.04 vs. 1.08, 1.06 vs. 1.08). These analyses revealed robust AC→PFC interactions in the theta/alpha (4-14 Hz) and gamma (30-70 Hz) bands, while PFC→AC interactions were more prominent in the delta and theta (4-8 Hz) bands (Fig. 5C). These connectivity patterns were replicated in the second monkey (Supplementary Fig. 7).

Behavioral modulation of prediction and prediction error in AC and PFC

After characterizing prediction and prediction error during novelty detection, we next examined the modulatory effects of behavior by comparing neural responses between behavioral and non-behavioral (passive) conditions. In the behavioral condition, monkeys actively performed the novelty detection task, whereas in the passive condition, monkeys listened to the same auditory stimuli without any task requirement.

We first focused on predictive processing. In the behavioral condition, a representative PFC site exhibited robust oscillatory activity at approximately 2 Hz from 3.5 to 5 s (Fig. 6A, left panel), while this 2 Hz activity was markedly diminished during the passive condition (Fig. 6A, right panel). To assess regional specificity, we compared all 64 recording sites in each brain area (Fig. 6B). The behavioral

modulation of prediction-related activity was more pronounced in the PFC than in the AC, as further illustrated by site-by-site scatter plots (Fig. 6C). Statistical analysis revealed a significant difference between behavioral and passive conditions in the PFC ($F(1, 126) = 12.45$, $p < 0.001$, $\eta^2 = 0.05$, two-way ANOVA; Fig. 6C, bottom panel), but not in the AC ($F(1, 126) = 1.43$, $p = 0.23$, $\eta^2 = 0.01$; Fig. 6C, top panel). GC analysis revealed weaker connectivity between PFC and AC in the passive condition (Supplementary Fig. 8A) compared to the behavioral condition (Fig. 3A). Moreover, there were no significant temporal dynamics in either direction during the passive condition (Supplementary Fig. 8B), in contrast to the pronounced bidirectional dynamics observed during active task performance.

For prediction-error, example sites in both AC and PFC (Fig. 6D, left and right panels) showed less differentiated responses to deviant stimuli in the passive condition, in contrast to the distinct responses observed during the behavioral task (cf. Figs. 4A, B). Across both brain areas and in both monkeys, the tonotopic distribution of *F*-values was reduced under passive listening (Fig. 6E). Corresponding scatter plots demonstrated significantly stronger prediction-error responses during the behavioral condition ($p < 0.05$ for all comparisons, two-tailed paired *t*-test; Fig. 6F). Notably, GC analysis indicated significant information flow from AC to PFC in the theta and alpha frequency bands, suggesting the presence of stable feedforward connectivity even in the passive state (Supplementary Fig. 9).

Discussion

In this study, we investigated the neural dynamics of novelty detection in the auditory cortex (AC) and prefrontal cortex (PFC) of macaques performing a behaviorally relevant auditory oddball task. Our results revealed distinct repetition-related responses: while some AC sites exhibited repetition suppression, the majority of AC and PFC sites showed repetition enhancement, particularly in low-frequency (~2 Hz) oscillatory activity (Figs. 2A-E). These effects were quantified using linear fits of delta-band power, which demonstrated stronger facilitation in PFC than in AC (Fig. 2F). Granger causality (GC) analyses identified robust bidirectional interactions between AC and PFC, peaking around 2 Hz and within the delta band, reflecting coordinated predictive processing across regions (Fig. 3; Supplementary Figs. 3-4). Deviant tones evoked enhanced responses in both regions, with earlier onset in AC (Figs. 4A, C), while the overall magnitude of prediction-error responses was comparable (Fig. 4D). Deviant processing also led to increased GC in the AC→PFC direction, particularly in the delta and theta bands, accompanied by frequency-specific cross-regional coupling—delta-gamma from AC to PFC and delta-theta from PFC to AC (Fig. 5; Supplementary Figs. 6-7). Crucially, both prediction and prediction error signals were significantly amplified during active task engagement compared to passive listening, with stronger repetition-related enhancement, interareal connectivity, and deviance sensitivity observed under behavioral conditions (Fig. 6; Supplementary Figs. 8-9). These findings support a distributed and state-dependent model of predictive coding, in which AC encodes early sensory regularities and violations, while PFC integrates contextual information to guide top-down modulation.

Dual Modes of Prediction in the AC-PFC Circuit

Repetition suppression (RS) and repetition enhancement (RE) reflect complementary predictive plasticity mechanisms in auditory and prefrontal cortices. In AC, RS—observed in ~43% of electrodes—manifests as progressive attenuation of evoked responses to repeated tones (Figs. 2A, D), consistent with predictive coding models where redundant stimuli minimize prediction-error signaling in primary AC and subcortical nuclei [4,5,50,51]. In contrast, the remaining two-thirds of AC sites displayed robust repetition-enhancement: evoked amplitudes and phase-locked power at the stimulation rhythm (~2 Hz) rose monotonically (Fig. 2B, D). Similar facilitation—termed location-specific or context-specific enhancement—has recently been reported in marmoset and mouse AC [52,53] and is thought to store a short-term "prediction template" that sharpens temporal expectancy via the delta phase code [54]. PFC expressed the same dual motifs but was strongly biased toward enhancement: 76 % of electrodes showed progressive facilitation, often with a later build-up than in AC (Figs. 2C-F). This dominance aligns with evidence that medial PFC broadcasts precision-weighted predictions that increase auditory gain when behavioral relevance is high [37,55] and frontal networks maintain cross-modal predictive templates during working memory [55].

Notably, these effects are dynamically modulated by behavioral state. During passive listening, RE strength drops sharply in PFC (33% of average 2-Hz power slope decrease relative to behavioral condition) compared to AC (22%), accompanied by weakened PFC-AC low-frequency coupling (Supplementary Fig. 8). This parallels findings that task demands amplify frontal contributions to sensory processing [56,57], positioning PFC-driven RE as a mechanism for refreshing predictive templates during engagement. RS, conversely, dominates in passive contexts, favoring efficiency through reduced resource allocation. Such state dependence underscores a functional

dissociation: RS streamlines processing of predictable inputs, while RE prioritizes behaviorally salient signals through active cortical buffering.

The coexistence of RS and RE in overlapping regions supports a multiplexed predictive coding framework. RS in AC aligns with prediction-error minimization at sensory levels, whereas RE in PFC reflects precision-weighted model updating [50]. The delta-phase-mediated RE in AC and task-dependent PFC facilitation suggest temporal coding and fronto-sensory interactions jointly refine predictive accuracy. These findings advance our understanding of how the brain balances efficiency (via RS) and precision (via RE) across hierarchical networks, adapting to environmental demands through dynamic AC-PFC interactions. Future work should explore how these mechanisms generalize to naturalistic contexts and clinical populations with disrupted predictive processing.

The GC patterns observed during standard tone repetitions reveal a structured interplay between AC and PFC that supports predictive maintenance. Bidirectional interactions peaked at ~2 Hz (Figs. 3A-B), aligning with the stimulation rhythm and phase-locked delta oscillations in both regions (Figs. 2E-F). This delta-band coherence suggests that AC and PFC synchronize to encode temporal regularities, with AC→PFC and PFC→AC pathways jointly reinforcing the stability of predictive templates. The dominance of delta frequencies in these interactions (Figs. 3B-C) resonates with theories proposing that low-frequency oscillations coordinate hierarchical predictions [39,54,58], where AC may relay sensory-derived temporal statistics to PFC, while PFC reciprocally modulates AC gain to prioritize behaviorally relevant patterns [37].

Notably, GC strength during standards was state-dependent: active task engagement strengthened PFC→AC coupling compared to passive listening

(Supplementary Fig. 8), paralleling the heightened RE prevalence in PFC during behaviorally relevant contexts. This asymmetry implies that top-down signals from PFC amplify sensory predictions when task demands require sustained attention to auditory regularities. Conversely, passive listening weakened PFC→AC influence, favoring bottom-up AC-driven interactions. Such flexibility aligns with predictive coding frameworks where precision weighting—modulated by behavioral relevance—adjusts the balance between top-down predictions and bottom-up sensory evidence [50,59].

The persistence of delta-band GC across repetition rates (Supplementary Fig. 4) further underscores its role in maintaining temporal predictions. Unlike higher-frequency interactions (e.g., gamma), which are often linked to local processing or prediction-error signaling [60], delta oscillations may act as a scaffold for cross-regional prediction maintenance. This is consistent with studies showing that delta-phase coding in AC sharpens temporal expectations [54,61], while PFC leverages these rhythms to sustain working memory representations [62]. Together, these findings suggest that AC-PFC delta synchrony during standards reflects a dynamic "prediction loop" that stabilizes auditory regularities and optimizes resource allocation for anticipated inputs.

Prediction-error hierarchy and AC-PFC communication

Our findings delineate a hierarchical framework for prediction-error processing within the auditory system, emphasizing the dynamic interplay between the AC and PFC. Deviant tones elicited significant neural responses in both regions; however, the temporal dynamics differed notably. Specifically, divergence from standard responses occurred approximately 30~100 milliseconds earlier in the AC compared to the PFC (Figs. 4A-C; Supplementary Figs. 5A, B). This temporal precedence aligns with prior

studies indicating that prediction-errors emerge earlier in lower-order auditory areas and subsequently propagate to higher-order regions, supporting the hierarchical nature of predictive processing [63,64]. Despite the earlier onset in the AC, the magnitude of the prediction-error responses, as quantified by peak *F*-values, did not significantly differ between the AC and PFC (Fig. 4D). This suggests that while the AC rapidly detects deviations, the PFC may play a crucial role in amplifying or integrating these signals, potentially reflecting its involvement in higher-order cognitive processes such as attention and decision-making [65].

GC analyses further elucidated the directional flow of information during deviant processing. We observed a pronounced increase in GC from the AC to the PFC within the delta and theta frequency bands, commencing within 100 milliseconds post-stimulus onset (Fig. 5A). This pattern indicates a feedforward transmission of prediction-error signals from sensory to frontal regions. Subsequently, enhanced GC from the PFC to the AC in similar frequency bands suggests a feedback mechanism, potentially involved in updating predictive models based on the detected discrepancies [63]. Moreover, the observed increase in PFC-to-AC GC following deviant detection suggests a rapid adjustment of predictive templates, aligning with studies that associate frontal feedback with the updating of expectations in response to unexpected auditory events [63]. Notably, AC sites exhibiting the most substantial early prediction-error responses also demonstrated the greatest enhancement during standard sequences (Figs. 2E and 4C), indicating a possible shared mechanism that modulates both the encoding of regularities and the detection of deviations.

Crucially, these prediction-error dynamics were strongly modulated by behavioral engagement. During active task performance, both AC and PFC exhibited significantly stronger deviant responses and broader spatial differentiation of

prediction-error signaling compared to the passive condition (Figs. 6D-F). Granger causality analysis confirmed that GC strength in delta and theta bands was markedly enhanced during behavior, particularly in the AC→PFC direction, suggesting increased feedforward signaling of errors when the task was behaviorally relevant (Supplementary Fig. 9). These findings are consistent with theories proposing that prediction-error signaling is weighted by task demands and attentional context [66], and they highlight the role of behavioral relevance in gating the magnitude and directionality of prediction-error flow across cortical networks.

Collectively, these results support a bidirectional model of auditory predictive processing: the AC rapidly identifies sensory discrepancies and conveys this information to the PFC, which integrates contextual and behavioral relevance before transmitting refined predictions back to the AC. This dynamic interplay facilitates adaptive auditory perception and aligns with predictive coding theories that emphasize hierarchical and reciprocal neural interactions.

Methods

Experimental model and surgical procedures

Our study involved two 7-year-old male rhesus monkeys (C and X), each weighting between 5.5 and 7 kg. The experimental protocols and procedures were strictly in accordance with the principles of the Guide for Care and Use of Laboratory Animals of the Directive of the European Communities (86/609/CEE, 2003/65/CE, and 2010/63/UE) and the Regulations for the Administration of Affairs Concerning Experimental Animals, approved by the State Council of the People's Republic of China (GB 14925-2010) and the Bioethics Committee of Zhejiang University (ZJU20200148).

Two 64-channel electrode arrays (E64-2500-50-200, NeuroNexus Technologies Inc., Michigan, USA) were implanted over the subdural regions of the left auditory cortex (AC) and prefrontal cortex (PFC) in each monkey. Detailed surgical procedures and ECoG recording methods have been described in our previous published study [67]. Aseptic surgical techniques were employed for the implantation of the headpost and ECoG array. Premedication included the administration of ketamine (50 mg/kg) and medetomidine (0.03 mg/kg). Subsequently, the monkeys were intubated and connected to an artificial respirator (A.D.S.1000, Engler Engineering Corp., FL) to maintain a stable body temperature of 37°C using an electric heating mat. Continuous monitoring of vital signs, including oxygen saturation, heart rate, and end-tidal CO□ (Surgi Vet, Smiths Medical PM Inc., London, UK), allowed for precise adjustments in anesthesia levels. The implantation process required securing the skull within a

stereotactic frame (Narishige, Tokyo, Japan). After administering lidocaine, we carefully removed skin and muscles in the target area. A titanium headpost (Gray Matter Research, MT) was securely affixed to the skull using resin and bone screws. Craniotomy and durotomy procedures were performed with the assistance of a microscope (Ophthalmo-Stativ S22, Carl Zeiss Inc., Oberkochen, Germany) equipped with a CMOS color camera (TS-CA-130MIII, MeCan Imaging Inc., Saitama, Japan). Following the implantation of the ECoG array, we sealed the surgical site with the dura mater, bone flap, and skin, and covered the exposed skull area with resin. Postoperatively, the monkeys received ketoprofen for three days and antibiotics for one week to ensure their well-being and minimize the risk of infection.

ECoG recording

The ECoG electrodes used in this study had a diameter of 0.2 mm, with gold surfaces exposed on a 2 × 2 cm polyimide substrate. The electrode impedances, measured at 1 kHz, ranged from 20 to 50 kΩ, and the inter-electrode distance was maintained at 2.5 mm. To ensure precise placement, we utilized preoperative MRI scans to determine target locations and determine appropriate craniotomy sizes. Additionally, we positioned a gold reference electrode near the ECoG array within the subdural space, oriented towards the dura. Lead wires originating from both the ECoG array and reference electrodes were connected to micro connectors (ZIF-Clip 64, Tucker-Davis Technologies, TDT, Alachua, FL). These connectors were housed within a titanium chamber affixed securely to the skull using resin. To capture neural signals, we amplified and filtered the ECoG signals with a Butterworth filter in the

range of 0.5–300 Hz using a differential amplifier (RZ5, TDT).

Sound stimulation

Experiments were conducted within a sound-proof room, where the monkey was seated in a chair with its head fixed, hands placed on a button, and right ear oriented towards a speaker (LS50, KEF, UK). All acoustic stimuli were digitally generated with a computer-controlled Auditory Workstation (RZ6, TDT) at a sampling rate of 100 kHz and delivered through the speaker on the contralateral (right) side of the ECoG implantation. To ensure accuracy, we calibrated sound pressure levels using a ¼-inch condenser microphone (Brüel & Kjær 4954, Nærum, Denmark) and a PHOTON/RT analyzer (Brüel & Kjær, Nærum, Denmark).

The sound stimuli involved in this study were complex tones composed of 6 harmonics, described by the equation:

$$y(t) = \sum_{i=1}^{6} \frac{1}{6} \sin\left[2\pi \left(2^{i} f_0\right) t\right]$$

where, t represents time and f_0 is the base frequency of the complex tone. The base frequency of the standard sound was set to 245 Hz. The base frequency of the deviant sound was altered relative to the standard sound by a ratio λ, such that $f_{dev} = f_{std} \times \lambda$. In deviant trials, λ was randomly selected from the values 1.02, 1.04, 1.06, and 1.08. For both standard and deviant complex tones, the duration was fixed at 100 ms and the sound pressure level was calibrated and maintained at 60 dBSL.

Behavioral task

The monkeys were trained to perform a novelty detection task based on oddball stimulation [68], as illustrated in Figure 1A. In each trial, the monkey initiated the trial

by pressing a button. Two seconds after the button press, an oddball sequence of 8-11 complex tones was presented at a rate of 2 Hz (500-ms inter-stimulus interval [ISI], defined as the time from the onset of one sound to the onset of the next sound). A 5-s break time was set between trials, during which button presses were invalid. The initial sounds in the sequence were standard (consistent frequency), while the final target sound either differed in frequency from the previous sounds (deviant trial, red, Fig. 1A) or was identical (control trial, black, Fig. 1A). The monkey was required to press the button within 600 ms after the onset of the deviant sound to receive a water reward (Fig. 1A). This time constraint effectively eliminated the possibility of the monkey pressing the button merely because it was the final stimulus in the block, given that the minimum reaction time typically exceeds 200 ms. Trials were categorized based on the frequency ratio between the deviant and standard sounds into five groups: 1 (control), 1.02, 1.04, 1.06, and 1.08. These groups were presented randomly, with each being repeated 40-50 times during a single recording session. The number of standard stimuli in each trial randomly varied between 7 and 10 to prevent button presses based solely on the fixed sequence length. Following the behavioral session, a non-behavioral session was conducted, during which a baffle was placed between the button and the monkey's hands to prevent any motor responses. An additional behavioral session with 400-ms ISI was also recorded for each monkey.

We assessed the monkey's behavior based on two criteria. 1) Correct Hit (Deviant Identification): The monkey was required to correctly identify the deviant stimulus,

achieving an accuracy rate of at least 80% (corresponding to a button-pressing ratio greater than 0.8) for the largest difference condition. 2) Correct Rejection (Absence of Deviant): In trials where no Deviant stimulus occurred, the monkey was expected to correctly reject its absence, achieving a high accuracy rate of at least 90% (indicated by a button-pressing ratio less than 0.1) for the control condition. Only those recording sessions that met both criteria were included in the analysis. A total of five behavioral sessions and four non-behavioral sessions were recorded for each monkey.

Quantification and statistical analysis

Data processing was performed using custom MATLAB codes (MATLAB R2023b, The MathWorks Inc., Natick, MA, USA) based on the FieldTrip toolbox (https://www.fieldtriptoolbox.org/) [69].

Data preprocessing

The ECoG data were first down sampled to 500 Hz and then underwent band-pass filtering (0.1-200 Hz) and notch filtering (50 Hz). The filtered data were segmented from 3 s before and 7 s after the first sound onset of each trial. To reduce noise, independent component analysis (ICA) was performed using the 'runica' function from the FieldTrip toolbox. Components were retained or rejected based on their topographic distribution and variance.

Following ICA, signal re-referencing was performed in three steps. First, common average referencing (CAR) was applied by subtracting the common average of the trial data from the channels within the same array. This step reduced signal differences between arrays due to variations in electrode impedance and other

array-specific factors. Next, the data were re-referenced by subtracting the average signal from the four horizontally and vertically adjacent electrodes (orthogonal source derivation). This re-referencing mitigated issue related to common reference and volume conduction, improving the spatial localization of signals. Finally, the data were normalized by the temporal standard deviation of the amplitude to ensure equal weighting of data across electrodes and trials. The re-referenced data were then averaged across recording sessions for response comparison and time-frequency analysis of the raw wave.

For Granger causality (GC) analysis, an additional procedure was applied to the re-referenced data. The average event-related potential (ERP) was subtracted from individual trials to remove evoked potentials locked to trial events (e.g., stimulus onsets and offsets). This step isolated internally generated components, such as induced oscillations, that were not phase-locked.

Time-frequency analysis

Time-frequency analysis was conducted on both the re-referenced and ERP-subtracted data using the MATLAB 'cwt' function. Morlet wavelets with default parameters (time-bandwidth product = 5) were employed as the analytic wavelets.

The time-frequency response (TFR) during standard sound presentations was computed using the integrated ERP data for prediction analysis. ERPs from trials with different standard sound numbers were computed separately and then combined using a weighted average. To mitigate edge effects from the cone of influence (COI) in wavelet transformation, data were first extended to 10 s with zero padding on both

sides, applied with wavelet transformation and then trimmed back to the original length. For GC analysis, TFR was computed at the single-trial level. Specially, for prediction GC analysis, only the standard sound period of each trial was included in the TFR computation, spanning from the onset of the first sound to just before the onset of the deviant sound (or to an ISI period following the last standard sound in control trials). For prediction-error GC analysis, data of 1 s after the onset of the last deviant/standard sound were used for TFR computation.

Prediction suppression and enhancement analysis

Prediction suppression and enhancement were assessed by averaging spectral power over a frequency band centered around the repeat rate (-0.2 Hz to 0.2 Hz relative to the repeat rate, 1.8-2.2 Hz for a 500-ms ISI and 2.3-2.7 Hz for a 400-ms ISI, Fig. 2E and Supplementary Fig. 2C). To estimate changes of prediction signals over time, the averaged spectral power of the repeat rate was fitted within the standard sounds of orders 4 to 9 (Fig. 2E and Supplementary Fig. 2C). Slopes of these linear fits were compared between brain areas (AC vs. PFC, Fig. 2F and Supplementary Fig. 2D), ISI conditions (400-ms vs. 500-ms, Supplementary Figs. 2E-F), and behavioral contexts (behavioral vs. non-behavioral, Figs. 6B-C).

Granger causality (GC) analysis

GC is a statistical test used to assess the predictive influence of one time series on another, specifically to determine whether past values of one series contain statistically significant information that improves the prediction of the future values of another series. In this study, nonparametric GC was employed, where the transfer

matrix and covariance matrix of the residuals were estimated by factorizing the cross-spectral density matrix. The cross-spectral density matrix for all electrode pairs between the AC and PFC was computed using wavelet-transformed spectra. For GC analysis of prediction, all trials without button presses during the standard sound period were included, spanning from the onset of the first sound to just before the onset of the deviant sound (or to an ISI period following the last standard sound in control trials). Trials with different standard sound numbers (7-10) were computed separately. For GC analysis on prediction-error, all trials from non-behavioral sessions and successful trials from behavioral sessions were included, spanning from the onset of the last sound to 1s post-stimulus. Nonparametric GCs were computed in both directions (AC→PFC and PFC→AC) for all electrode pairs per frequency bin (72 bins between 0.6 and 70 Hz) and time bin (with a step of 2 ms). Baseline GCs (from -3 s to -2.5 s, relative to the first sound onset) were subtracted from the results for subsequent analyses.

Frequency bins were assigned into 5 frequency bands: δ (0.6-4 Hz), θ (4-8 Hz), α (8-14 Hz), β (14-30 Hz), and γ (30-70 Hz). GC data were then averaged within each frequency band.

To estimate the average information flow at individual electrodes under different conditions, GC maps were created by averaging the GCs between each electrode in one area (AC or PFC) and all electrodes in the other area. This calculation was performed for each direction (AC→PFC and PFC→AC), each frequency ratio (1, 1.02, 1.04, 1.06, and 1.08), each frequency band (2 Hz, δ, θ, α, β, and γ), and each

time window (overlapped, with a 100-ms bin size and a 50-ms step).

To assess the change in information flow between the AC and PFC over time in prediction GC analysis, we calculated Spearman's rank correlation of the GCs across time bins (from sound orders 5 to 6, e.g., 2-2.5 s for 500-ms ISI) for each electrode under each standard sound number condition. Topographic maps of Spearman's ρ, averaged across all standard sound number conditions (7-10), were plotted for each frequency band in both directions. Electrodes showing significant correlations ($p < 0.05$, [FDR] corrected for electrodes) across all sound number conditions were highlighted with 'x' (Fig. 3C and Supplementary Figs. 3-4).

For prediction-error analysis, a differential GC map was created by subtracting the GC map for the standard frequency ratio (i.e., 1) from that for a deviant frequency ratio (e.g., 1.08). To assess the topographic stability of the differential GC maps among deviant conditions, we calculated cross-period correlation matrices of the differential GC maps (Fig. 5C and Supplementary Figs. 7 and 9) between each pair of deviant conditions (1.04, 1.06, and 1.08) in each frequency band for each monkey under both behavioral and non-behavioral contexts. Deviant frequency ratio of 1.02 was excluded from this analysis for inadequate successful trials. The cross-period correlation matrix was defined as the Spearman's rank correlation between the differential GC maps of two deviant conditions. The results were considered significantly consistent when $p < 0.05$ (uncorrected) for all condition pairs (1.04 vs. 1.06, 1.04 vs. 1.08, and 1.06 vs. 1.08) and for both monkeys.

Statistical analysis

Spearman's ρ and its p-value (right tail) were calculated in the following analysis: 1) to assess the change in information flow between the AC and PFC over time in prediction GC analysis (Fig. 3C, Supplementary Figs. 3, 4C, and 8B); 2) to assess the topographic stability of the differential GC maps among deviant conditions (Fig. 5C, Supplementary Figs. 7 and 9).

Two-way ANOVAs were performed to assess whether the slopes of the linear fits of spectral power varied significantly across brain areas (Fig. 2F and Supplementary Fig. 2D), behavioral contexts (Fig. 6C), and between monkeys. The effect size of an N-way ANOVA was quantified using partial eta squared (η^2):

$$\eta_k^2 = \frac{SS_k}{SS_k + SS_{error}}$$

where k denotes the k-th factor in the ANOVA, SS_k represents the sum of squares for the k-th factor, and SS_{error} is the sum of squares of the residual term. A value of 0.01 for η^2 implies a small effect, while 0.06 for a medium effect and 0.14 for a large effect.

Two-tailed Mann-Whitney U tests were conducted for comparing the first significant time and maximum F-values between brain areas (Figs. 4C-D). The effect size of a Mann-Whitney U test was quantified using rank-biserial correlation (r):

$$r = \frac{|Z|}{\sqrt{n_1 + n_2}}$$

where Z is the standard test statistic (z-scored) from the Mann-Whitney U test, and n_1 and n_2 are sample sizes of the two independent groups. A value of 0.1 for r implies a small effect, while 0.3 for a medium effect and 0.5 for a large effect.

Two-tailed paired t-tests were conducted for comparing the maximum F-values

under different behavioral contexts (Fig. 6F). The effect size of a paired t-test was quantified using Cohen's *d*:

$$d = \frac{\overline{X} - \overline{Y}}{\sqrt{\frac{1}{N-1}\sum_{i=1}^{N}\left(X_i - Y_i - \left(\overline{X} - \overline{Y}\right)\right)^2}}$$

where d represents Cohen's d. X and Y are the paired samples with a total number of N. X_i and Y_i are the ith elements from the paired samples. $\overline{X}$ and $\overline{Y}$ are mean values of the samples. A value of 0.2 for *d* implies a small effect, while 0.5 for a medium effect and 0.8 for a large effect.

Bayesian statistical analyses were conducted to quantify evidence for the null hypothesis across different types of comparisons. For pairwise comparisons, we used Bayesian paired-sample or independent-sample *t*-tests with a Jeffreys-Zellner-Siow (JZS) prior, as described by [70]. For group comparisons involving more than two levels, we employed Bayesian N-way ANOVA, using default Cauchy priors on effect sizes [71]. All Bayes factors (BF_{10}) were computed using the BayesFactor toolbox [72] for MATLAB. A BF_{10} greater than 1 indicates evidence in favor of the alternative hypothesis, whereas a BF_{10} less than 1 indicates evidence in favor of the null.

To determine whether the neural responses differed significantly across the five frequency ratio conditions (Figs. 4A-B, 6D), we performed a non-parametric cluster-based permutation test using the FieldTrip toolbox. This test controls for multiple comparisons across time (and optionally channels) by identifying clusters of adjacent significant effects and assessing their likelihood under the null hypothesis. A two-tailed test was employed using an *F*-statistic appropriate for comparing more than

two independent conditions. The analysis proceeded as follows: 1) Data aggregation. For each participant and each of the five frequency ratio conditions, event-related responses were averaged across trials, resulting in a time-resolved representation of the evoked signal per condition. 2) First-level statistical testing. At each time point (and, if relevant, each sensor or channel), an *F*-test was performed across the five conditions to evaluate whether there was a main effect of frequency ratio. This yielded an *F*-value for each sample. 3) Neighbor definition. Spatial clustering required the definition of neighboring channels. In this analysis, neighbor channels were defined as orthogonal channels, that is, sensors positioned at adjacent locations on the ECoG array in orthogonal directions. This spatial adjacency allowed the test to form physiologically plausible spatiotemporal clusters of activity. 4) Cluster formation. Samples where the *F*-values exceeded a threshold corresponding to $p < 0.05$ (uncorrected) were selected as candidates for clustering. Clusters were formed by grouping temporally and spatially adjacent significant samples based on the defined neighbor structure. 5) Cluster-level statistic. For each cluster, the sum of the *F*-values within the cluster was calculated, resulting in a single cluster-level statistic per cluster. 6) Permutation procedure. To evaluate the significance of the observed clusters, the condition labels were randomly shuffled across trials, and the same clustering procedure was applied to each permutation. This process was repeated 1,000 times, each time recording the largest cluster-level statistic to build a reference distribution under the null hypothesis. 7) Significance testing. The observed cluster-level statistics from the original (unpermuted) data were then compared to the distribution of

maximum cluster-level statistics obtained from the permutations. A cluster was considered significant if its cluster-level statistic fell in the extreme 2.5% of the null distribution on either tail (two-tailed test, $p < 0.05$ corrected for multiple comparisons). This method ensures control over the family-wise error rate while preserving sensitivity to temporally and spatially extended effects, making it well-suited for electrophysiological data with high temporal resolution.

To determine whether the mean GC for each electrode was significantly higher in the deviant condition than in the standard condition, a one-tailed permutation test was performed. First, we randomly shuffled the GCs between each electrode and all other electrodes in the other area across a deviant condition and the standard condition for each frequency band and each time window. Then, the differential GC for that electrode was calculated. These two steps were repeated 1000 times for each electrode under each deviant condition to generate a null distribution of the differential GC. The *p*-value was defined as the proportion of values in the null distribution greater than the actual differential GC, under the null hypothesis that the mean GC in the deviant condition was not greater than that in the standard condition. An electrode was considered significant if $p < 0.05$ for all three deviant conditions (1.04, 1.06, and 1.08).

Figure Legends

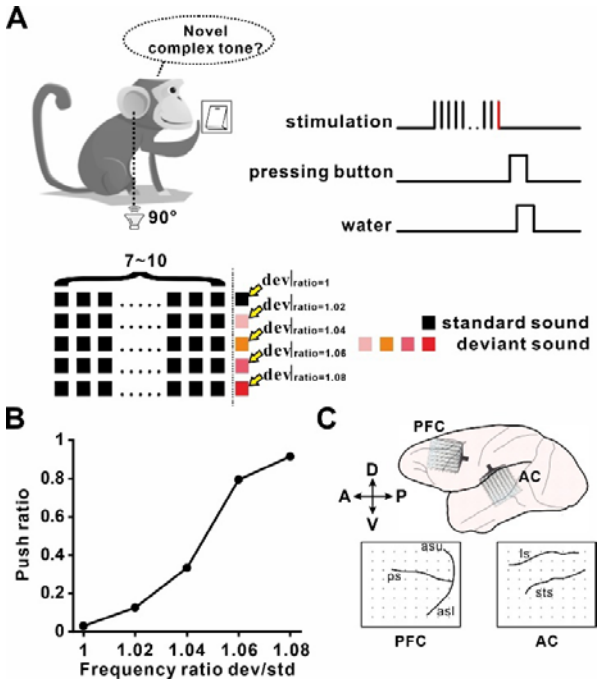

Figure 1. Experimental setup and task design for novelty detection in rhesus monkeys. (**A**) Schematic of the novelty detection task used in the experiment. The task involves presenting oddball stimuli consisting of a sequence of standard sounds (randomly ranging from 7 to 10 sounds), followed by a deviant sound, with an inter-stimulus interval (ISI) of 500 ms. The sounds are complex tones with a fixed duration of 100 ms and an intensity of 60 dBSL. The base frequency of the deviant sound is altered relative to the standard sound by ratios of 1 (control), 1.02, 1.04, 1.06, and 1.08. The monkey is required to press a button when a deviant sound occurs or hold on in a control trial to receive a water reward. (**B**) Button press ratio as a function of the frequency ratio between the deviant and standard sounds (an example from monkey C). (**C**) Illustration of the 64-channel ECoG arrays implanted on the auditory cortex (AC) and prefrontal cortex (PFC) of monkey C (asl: arcuate sulcus lower limb;

asu: arcuate sulcus upper limb; ps: principal sulcus; ls: lateral sulcus; sts: superior temporal sulcus; A: anterior; P: posterior; D: dorsal; V: ventral).

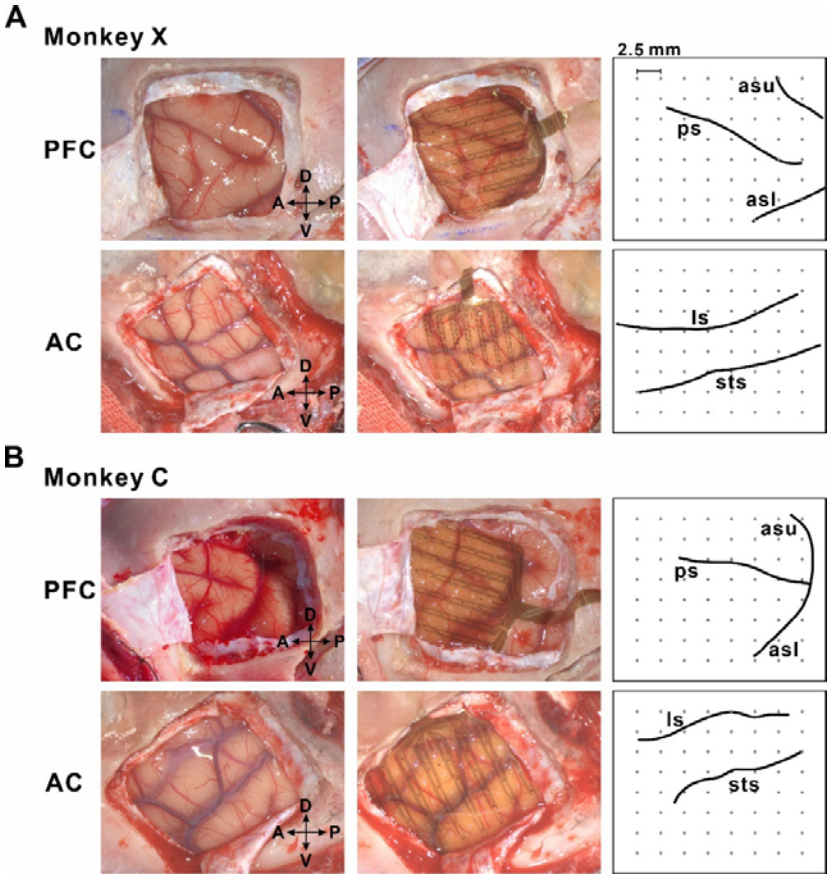

Supplementary Figure 1. ECoG array implantation. (**A**) ECoG array implantation (left: before implantation, middle: after implantation) in the PFC (top three) and AC (bottom three) of monkey X. Right schematic shows the channel numbers and the relative position of the electrode sites and sulcus (asl: arcuate sulcus lower limb; asu: arcuate sulcus upper limb; ps: principal sulcus; ls: lateral sulcus; sts: superior temporal sulcus; A: anterior; P: posterior; D: dorsal; V: ventral). (**B**) Same as (A) for monkey C.

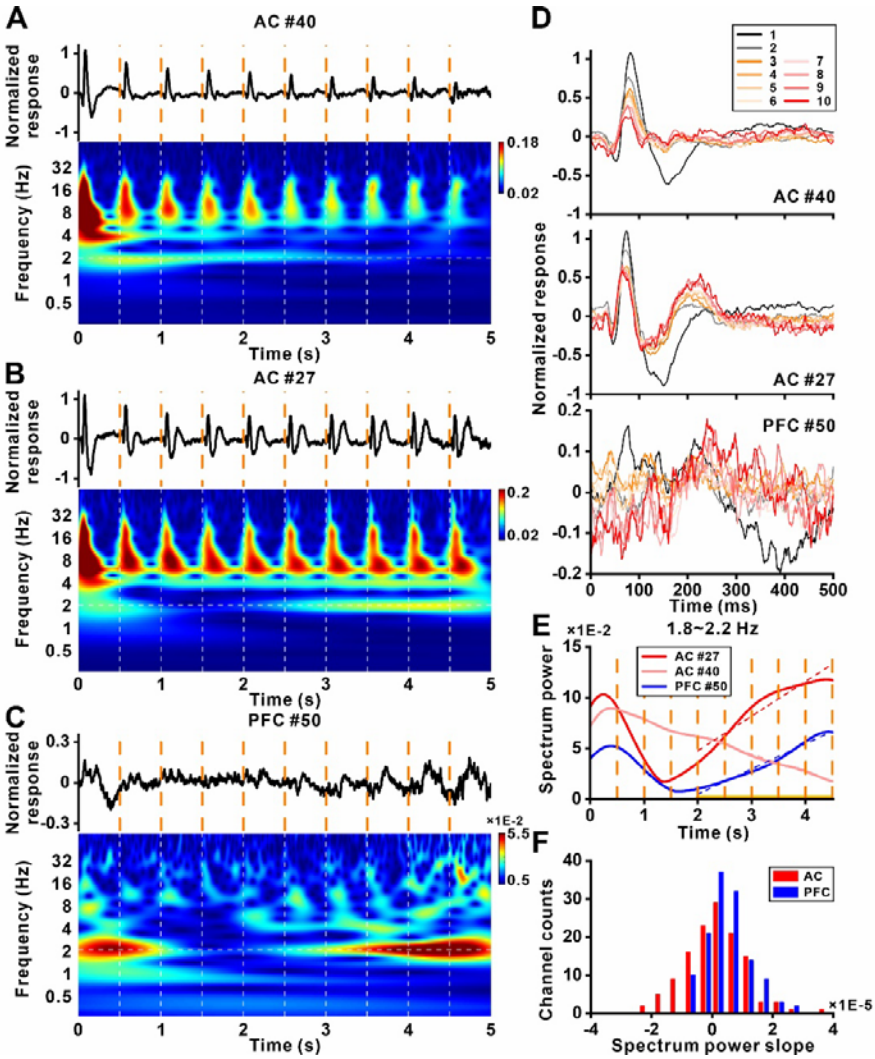

Figure 2. Suppression and enhancement of prediction in the AC and PFC of the monkey. (**A**) Example AC channel (#40) from monkey X showing prediction suppression. The top panel shows the normalized response averaged across trials, while the bottom panel shows the corresponding time-frequency response, where color represents spectrum power. Vertical dashed lines indicate the onset of each standard sound, and the horizontal dashed line marks the 2-Hz frequency corresponding to the 500-ms ISI. (**B-C**) Example channels (B: AC #27, C: PFC #50) from monkey X showing prediction enhancement. (**D**) Normalized responses of standard sounds from orders 1 to 10 for the three example channels. (**E**) Spectrum

power in the 2-Hz frequency band (1.8-2.2 Hz) for the example channels, showing changes over time. Vertical orange dashed lines indicate the onset of sounds. Slanted dashed lines represent linear fits from 2 to 4.5 s (corresponding to orders 5 to 9, indicated by the horizontal yellow line). (**F**) Histogram of the slopes from the linear fits in (E) for all channels in the AC and PFC for both monkeys.

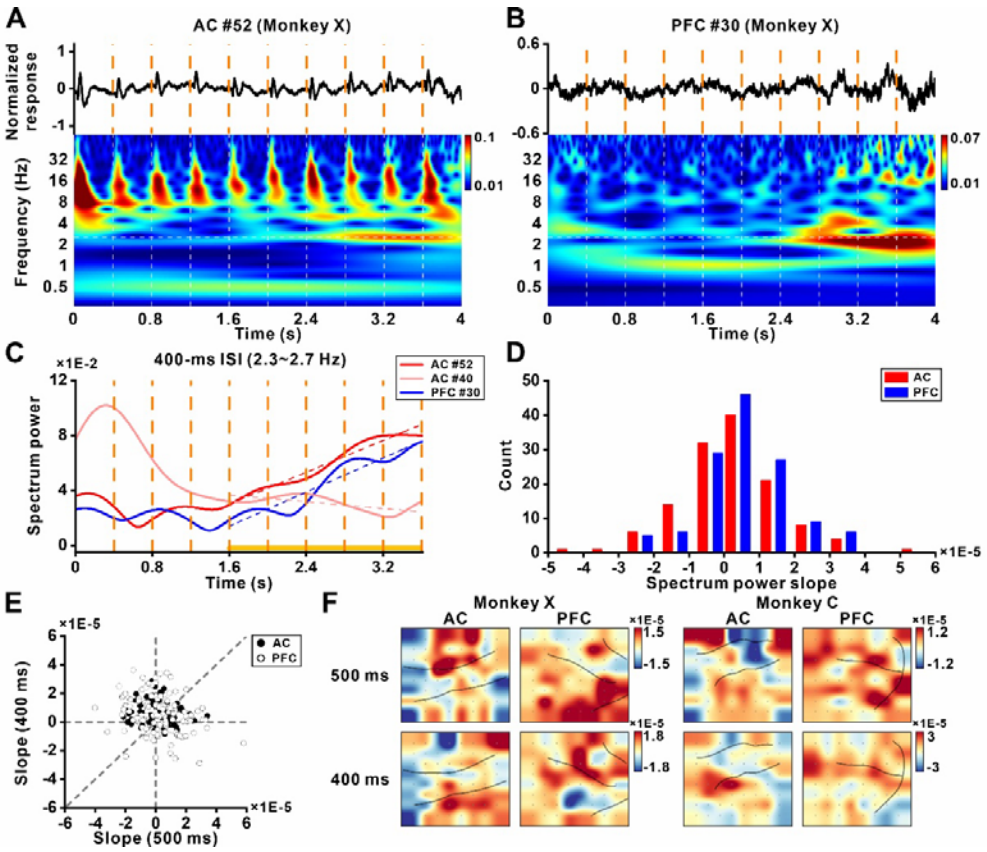

Supplementary Figure 2. Suppression and enhancement of prediction in the AC and PFC of the monkey under the 400-ms ISI condition. (**A-B**) Example channels from monkey X showing prediction enhancement under the 400-ms ISI condition. Vertical dashed lines indicate the onset of each standard sound, and the horizontal dashed line represents the 2.5-Hz frequency corresponding to the 400-ms ISI. (**C**)

Spectrum power in the 2.5-Hz frequency band (2.3-2.7 Hz) for the example channels, showing changes over time. Vertical orange dashed lines indicate the onset of sounds. Slanted dashed lines represent linear fits from 1.6 to 3.6 s (corresponding to orders 5 to 9, indicated by the horizontal yellow line). (**D**) Histogram of the slopes from the linear fits in (C) for all channels in the AC and PFC for both monkeys. Vertical dashed lines represent the mean values for AC (red for enhancement, light red for suppression) and PFC (blue for enhancement, light blue for suppression). No significant differences were observed between areas and between monkeys for both prediction suppression and enhancement (two-way ANOVA: $p = 0.08$ between areas, $p = 0.12$ between monkeys for suppression; $p = 0.44$ between areas, $p = 0.06$ between monkeys for enhancement). (**E**) Scatter plot comparing the slopes between the 500-ms and 400-ms ISI conditions. No significant correlation was observed between the two conditions for both areas ($p > 0.1$, Pearson's correlation). (**F**) Topographic comparison of slopes between the 500-ms and 400-ms ISI conditions. No significant correlation was observed between the two conditions in both areas for both monkeys ($p > 0.1$, Spearman's rank correlation).

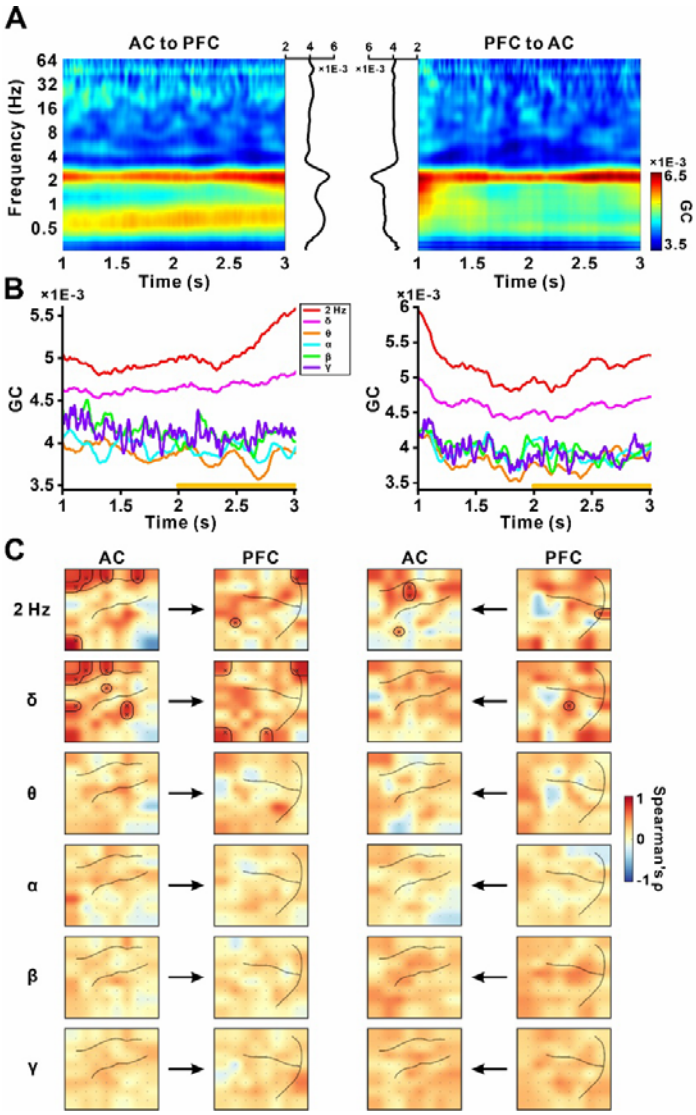

Figure 3. Enhancement of 2-Hz information flow between AC and PFC in prediction. (**A**) Time-frequency maps of Granger Causality (GC) spectrum, aligned to the onset of the first standard sound and averaged across all channels for monkey C. The example GC was computed using trials with a standard sound number of 8. Traces on the right and left display the GC averaged across time from 1 to 3 s, with a peak around 2 Hz. (**B**) GC for different frequency bands as a function of time, averaged across all channels for monkey C in both directions. Horizontal yellow bars indicate time window (2-3 s, orders 5-6) used for correlation calculation. (**C**)

Topographic maps of GC correlation over time under each frequency band for monkey C. Channels with significant correlation are circled in black and marked with 'x' (Spearman's rank correlation, $p < 0.05$, false discover rate [FDR] corrected for channels).

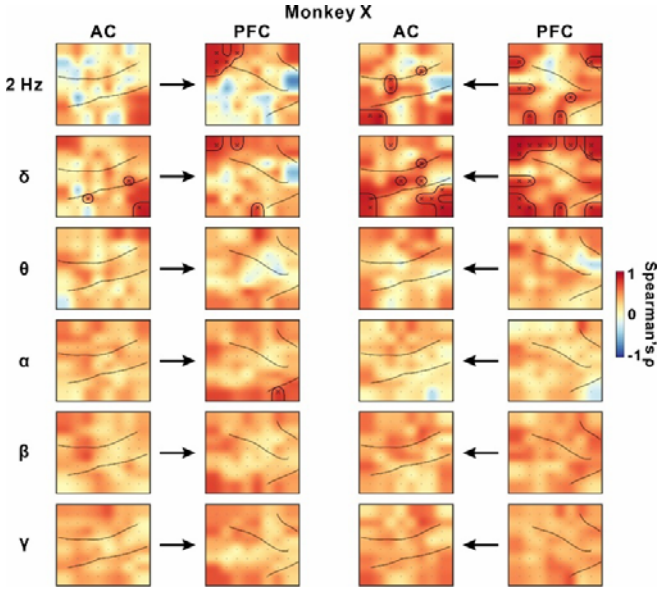

Supplementary Figure 3. Enhancement of information flow between AC and PFC in prediction in monkey X. Topographic maps of GC correlation over time under each frequency band for monkey X. Channels with significant correlation are circled in black and marked with 'x' (Spearman's correlation, $p < 0.05$, false discover rate [FDR] corrected).

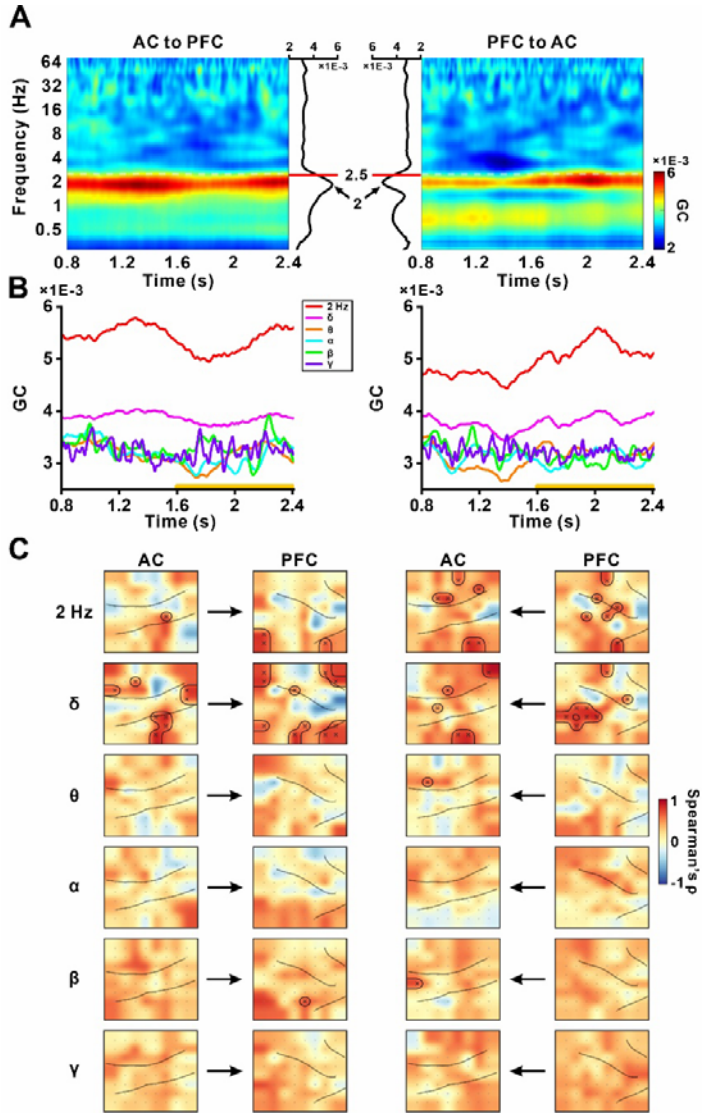

Supplementary Figure 4. 2-Hz as a characteristic frequency of prediction. (**A**) Time-frequency maps of GC spectrum, aligned to the onset of the first standard sound and averaged across all channels for monkey X under the 400-ms ISI condition. Traces on the right and left display the GC averaged across time from 0.8 to 2.4 s, with a peak around 2 Hz. White dashed and red solid vertical lines indicate 2.5 Hz corresponding to the 400-ms ISI. (**B**) GC for different frequency bands as a function of time, averaged across all channels for monkey X. Horizontal yellow bars indicate time window (1.6-2.4 s, orders 5-6) used for correlation calculation. (**C**) Topographic

maps of GC correlation over time under each frequency band for monkey C. Channels with significant correlation are circled in black and marked with 'x' (Spearman's rank correlation, $p < 0.05$, false discover rate [FDR] corrected).

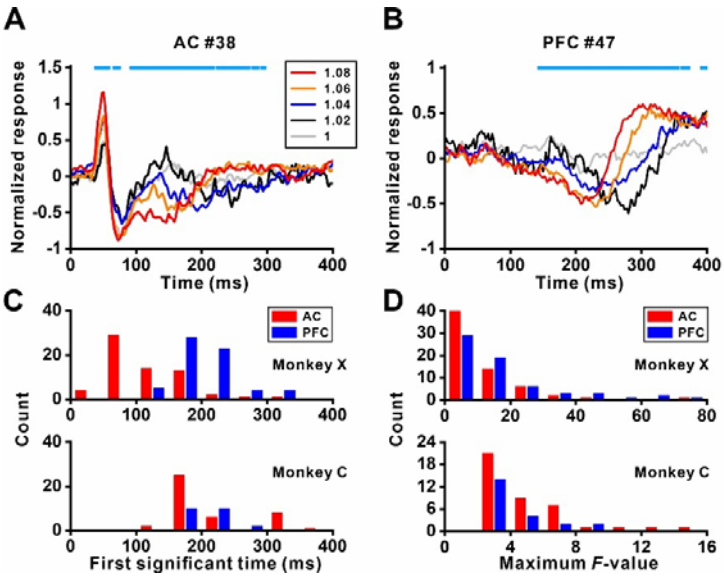

Figure 4. Prediction-error in the AC and PFC of the monkey. (**A**) Normalized responses for channel 38 in the AC of monkey X under five frequency ratios, aligned to the onset of the last sound and averaged across trials. Blue bars at the top indicate significant differences among the 5 traces (permutation test, $p < 0.05$, FDR corrected for channels and time bins). (**B**) Same as (A) but for channel 47 in the PFC of monkey X. (**C**) Histogram of time bins when the five traces start to show significant differences for each channel. The AC showed faster predictive error than PFC (two-way ANOVA: $p < 0.001$ between areas, $p < 0.01$ between monkeys). (**D**) Histogram of *F*-values averaged from 0 to 350 ms for each channel. No significant difference was found between areas for both monkeys (Kruskal-Willis test: $p = 0.13$ for monkey X, $p = 0.2$ for monkey C).

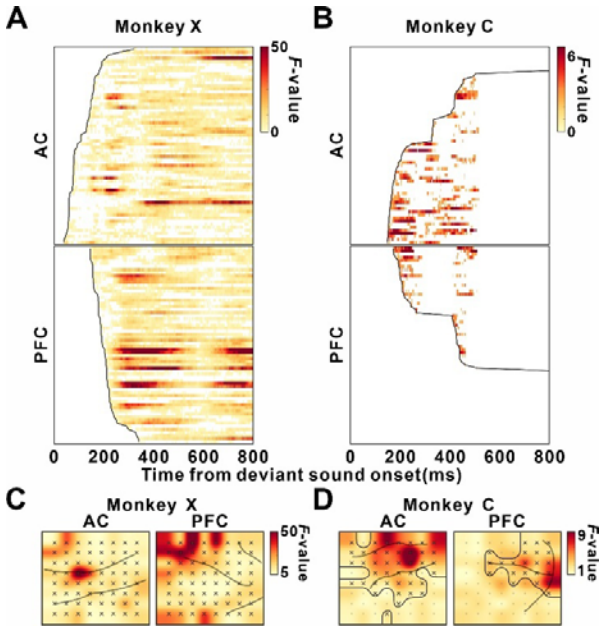

Supplementary Figure 5. Statistical results of prediction-error for all channels in both monkeys. (**A**) *F*-values of response comparisons among five frequency ratios for channels in the AC (top) and PFC (bottom) of monkey X, aligned to the onset of the last sound. Colors indicate significant time bins (permutation test, $p < 0.05$, FDR corrected for channels and time bins). The black curves indicate the boundaries of the first significant time bins. (**B**) Same as (A) but for monkey C. (**C**) Topographic maps of maximum *F*-values within 300 ms post-stimulus for AC (left) and PFC (right) of monkey X. Channels with significant difference (< 350 ms) are circled in black and marked with 'x'. (**D**) Same as (C) but for monkey C.

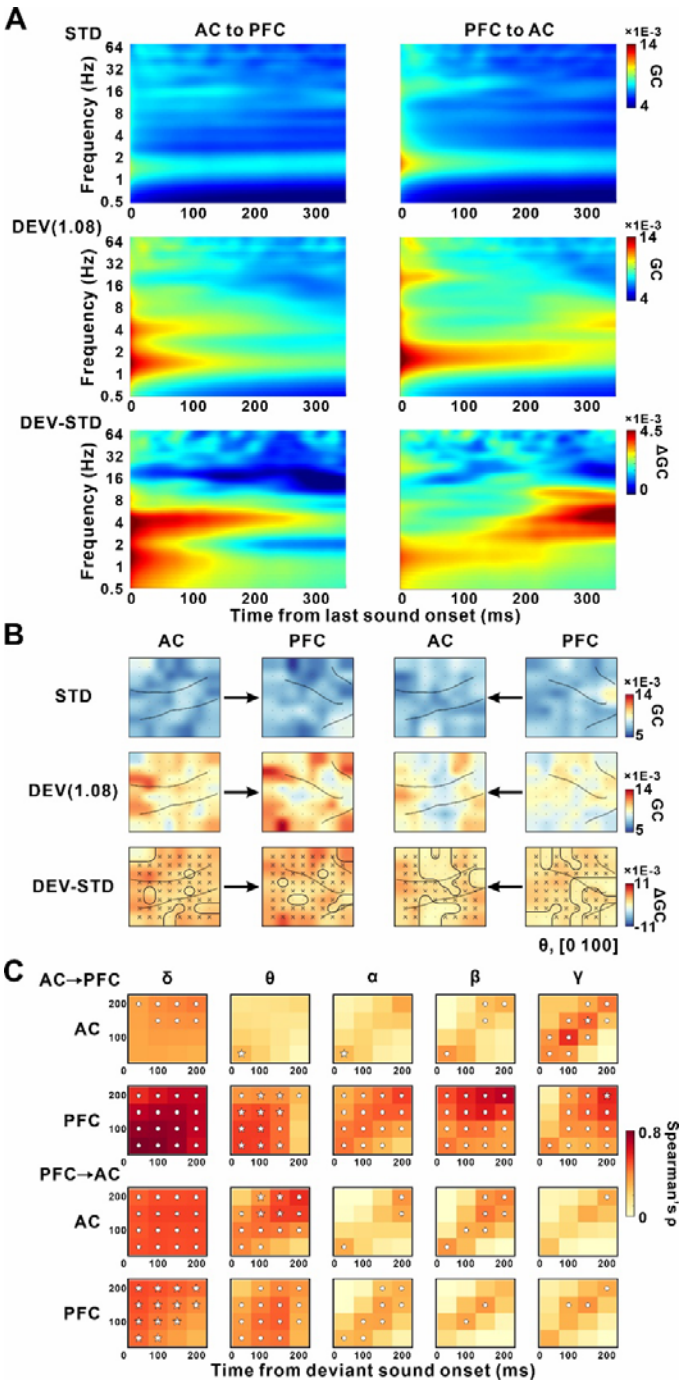

Figure 5. Information flow of prediction-error between the AC and PFC of the monkey. (**A**) Time-frequency maps of GC spectrum, aligned to the onset of the last sound and averaged across all channels for monkey X. Left: from AC to PFC. Right: from PFC to AC. Top: last sound as standard sound. Middle: last sound as deviant

sound with a frequency ratio of 1.08. Bottom: differential GC (deviant 1.08 subtracted by standard). (**B**) Topographic GC maps for standard (top), deviant (middle), and differential (bottom) conditions, averaged in the theta band and the [0 100] ms time window. Channels with significant differences between responses to deviant and standard sounds are circled in black and marked with 'x' (permutation test, $p < 0.05$, FDR corrected for channels). (**C**) Averaged cross-period correlation matrices of differential topographic GC maps between pairs in frequency ratios of 1.04, 1.06, and 1.08 for monkey X. The color scale indicates Spearman's ρ. Significant correlations for all pairs are indicated by dots for one monkey and by stars for both monkeys (Spearman's rank correlation, $p < 0.05$, uncorrected).

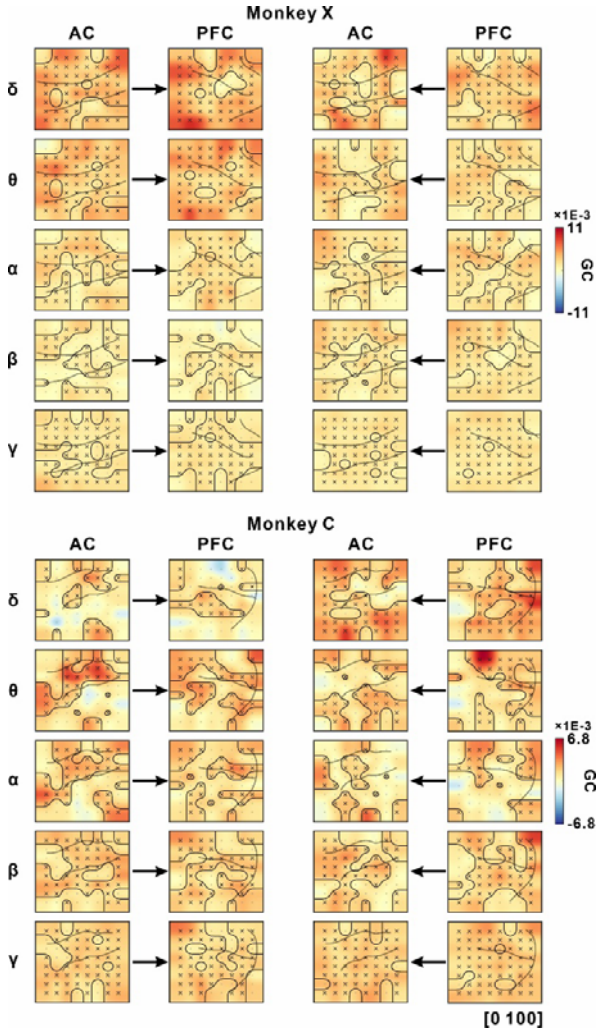

Supplementary Figure 6. Topographic differential GC maps for all frequency bands at time window [0 100] ms. Channels with significant differences between responses to deviant and standard sounds are circled in black and marked with 'x' (permutation test, $p < 0.05$, FDR corrected for channels).

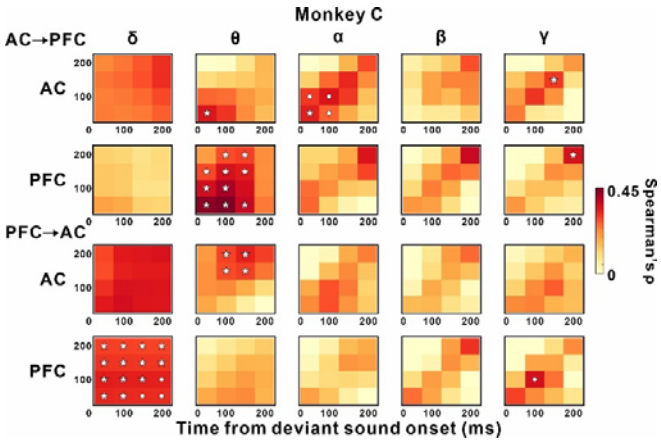

Supplementary Figure 7. Averaged cross-period correlation matrices of differential GC maps between pairs in frequency ratios of 1.04, 1.06, and 1.08 for monkey C. The color scale indicates Spearman's ρ. Significant correlations for all pairs are indicated by dots for one monkey and by stars for both monkeys (Spearman's rank correlation, $p < 0.05$, uncorrected).

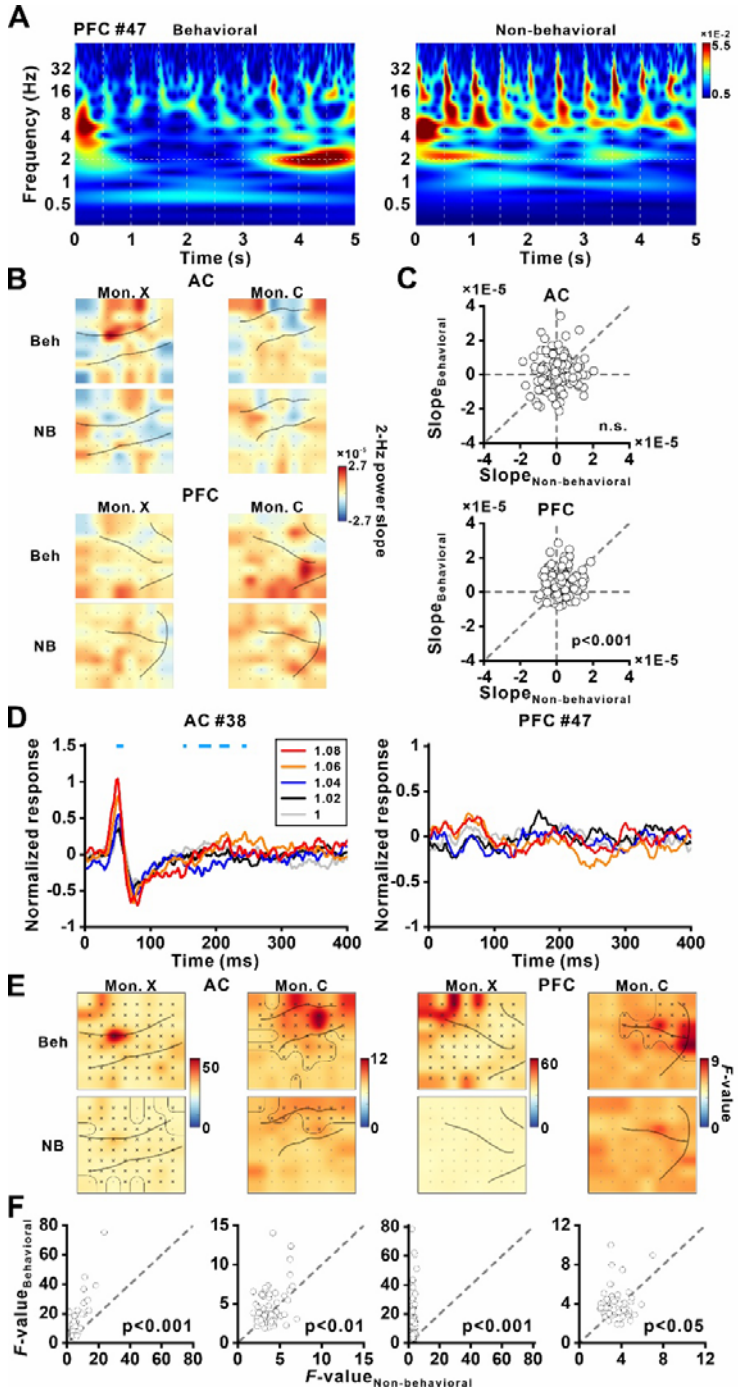

Figure 6. Behavioral context modulates prediction and prediction-error. (**A**) Time-frequency response of an example PFC channel during standard stimulus presentation under behavioral (left panel) and non-behavioral (right panel) contexts. (**B**) Topographic maps show the slopes of linear fits of 2-Hz power against time bins

(from 5th to 9th standard sounds) in AC and PFC under different contexts for both monkeys ('Beh' for behavioral and 'NB' for non-behavioral). (**C**) Scatterplots comparing slopes of 2-Hz power under behavioral and non-behavioral context, with each circle representing one recording site. The results of both monkeys are plotted together. Two-way ANOVA showed a main effect of behavioral context in PFC ($p < 0.001$) but not in AC (n.s., nonsignificant). No main effect of monkey was found for both areas. (**D**) Normalized responses for example channels from monkey X (same channel displayed in Figs. 4A-B) under five frequency ratios, aligned to the onset of the last sound and averaged across trials. Blue bars at the top indicate significant differences among the 5 traces (permutation test, $p < 0.05$, FDR corrected for channels and time bins). No significant difference was found in PFC. (**E**) Topographic maps of maximum *F*-values within 350 ms post-stimulus for two areas for both monkeys. Channels with significant difference (< 350 ms) are circled in black and marked with 'x'. (**F**) Scatterplots comparing maximum *F*-values under behavioral and non-behavioral contexts, with areas and monkeys aligned with (E). Two-tailed paired *t*-test showed significant increase of *F*-values under behavioral context for both areas and monkeys—AC of monkey X: $t(63) = 5.47$, $p < 0.001$, $d = 0.68$; AC of Monkey C: $t(63) = 2.51$, $p < 0.05$, $d = 0.31$; PFC of monkey X: $t(63) = 6.68$, $p < 0.001$, $d = 0.84$; PFC of monkey C: $t(63) = 2.1$, $p < 0.05$, $d = 0.26$.

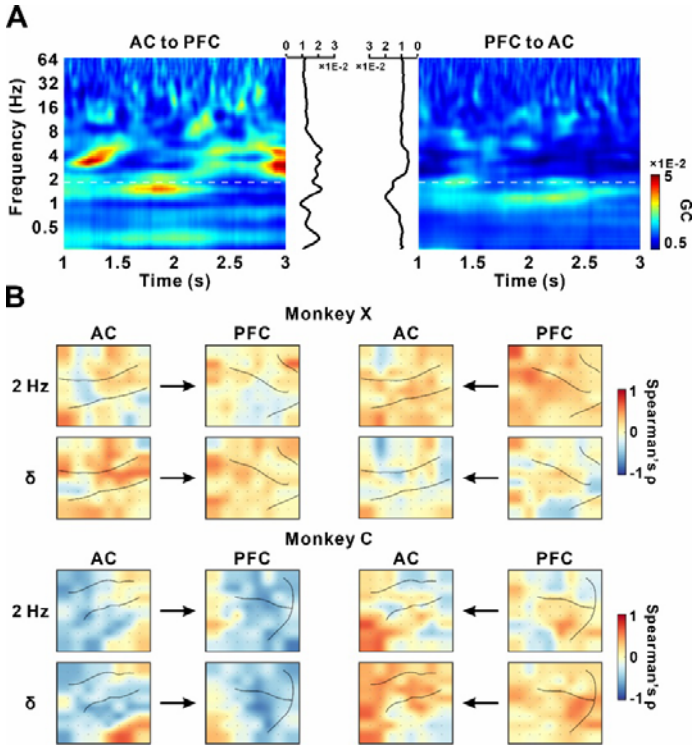

Supplementary Figure 8. Information flow between AC and PFC in prediction under non-behavioral context. (**A**) Time-frequency maps of Granger Causality (GC) spectrum, aligned to the onset of the first standard sound and averaged across all channels for monkey X. The example GC was computed using trials with a standard sound number of 8. Traces on the right and left display the GC averaged across time from 1 to 3 s. (**B**) Topographic maps of GC correlation over time under 2-Hz and δ frequency bands for both monkeys. No channels with significant correlation were found.

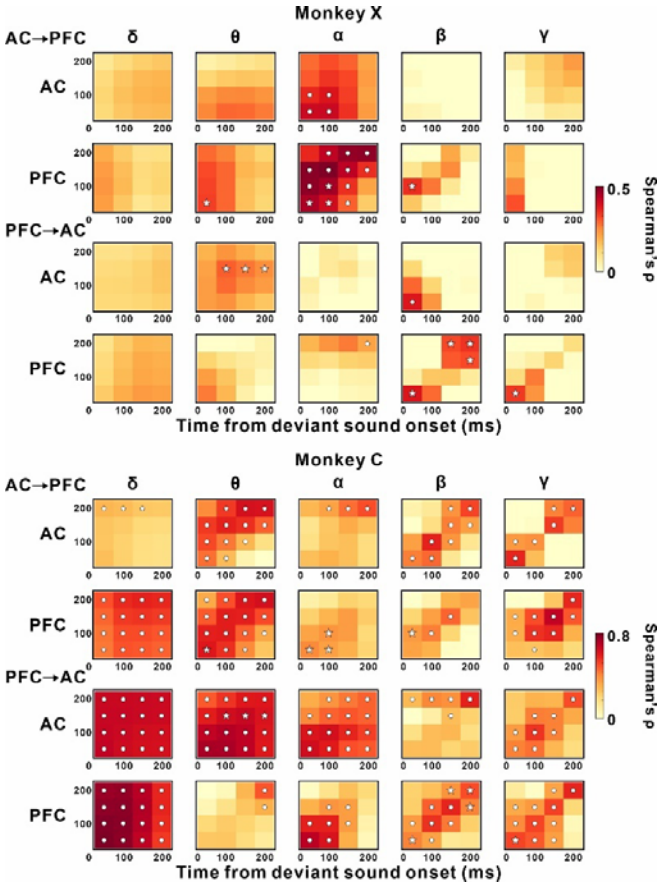

Supplementary Figure 9. Averaged cross-period correlation matrices of differential GC maps between pairs in frequency ratios of 1.04, 1.06, and 1.08 under non-behavioral context. The color scale indicates Spearman's ρ. Significant correlations for all pairs are indicated by dots for one monkey and by stars for both monkeys (Spearman's rank correlation, $p < 0.05$, uncorrected).

References

1 Fritz, J. B., Elhilali, M., David, S. V. & Shamma, S. A. Auditory attention—focusing the searchlight on sound. *Current Opinion in Neurobiology* **17**, 437-455 (2007). https://doi.org/https://doi.org/10.1016/j.conb.2007.07.011

2 Carandini, M. & Heeger, D. J. Normalization as a canonical neural computation. *Nat Rev Neurosci* **13**, 51-62 (2011). https://doi.org/10.1038/nrn3136

3 Waiblinger, C., McDonnell, M. E., Reedy, A. R., Borden, P. Y. & Stanley, G. B. Emerging experience-dependent dynamics in primary somatosensory cortex reflect behavioral adaptation. *Nat Commun* **13**, 534 (2022). https://doi.org/10.1038/s41467-022-28193-z

4 Yu, X.-J., Xu, X. X., Chen, X., He, S. & He, J. Slow recovery from excitation of thalamic reticular nucleus neurons. *J Neurophysiol* **101**, 980-987 (2009). https://doi.org/10.1152/jn.91130.2008

5 Song, P. R. *et al.* Adaptation in the Dorsal Belt and Core Regions of the Auditory Cortex in the Awake Rat. *Neuroscience* **455**, 79-88 (2021). https://doi.org/10.1016/j.neuroscience.2020.11.042

6 Nelken, I. Stimulus-specific adaptation and deviance detection in the auditory system: experiments and models. *Biol Cybern* **108**, 655-663 (2014). https://doi.org/10.1007/s00422-014-0585-7

7 Nelken, I. Processing of complex sounds in the auditory system. *Curr Opin Neurobiol* **18**, 413-417 (2008). https://doi.org/10.1016/j.conb.2008.08.014

8 Escera, C. & Malmierca, M. S. The auditory novelty system: an attempt to integrate human and animal research. *Psychophysiology* **51**, 111-123 (2014). https://doi.org/10.1111/psyp.12156

9 Zhang, F., Miller, C. A., Robinson, B. K., Abbas, P. J. & Hu, N. Changes across time in spike rate and spike amplitude of auditory nerve fibers stimulated by electric pulse trains. *J Assoc Res Otolaryngol* **8**, 356-372 (2007). https://doi.org/10.1007/s10162-007-0086-7

10 Willmore, B. D. B. & King, A. J. Adaptation in auditory processing. *Physiological Reviews* **103**, 1025-1058 (2022). https://doi.org/10.1152/physrev.00011.2022

11 Malmierca, M. S., Cristaudo, S., Pérez-González, D. & Covey, E. Stimulus-Specific Adaptation in the Inferior Colliculus of the Anesthetized Rat. *The Journal of Neuroscience* **29**, 5483 (2009). https://doi.org/10.1523/JNEUROSCI.4153-08.2009

12 Antunes, F. M., Nelken, I., Covey, E. & Malmierca, M. S. Stimulus-specific adaptation in the auditory thalamus of the anesthetized rat. *PLoS One* **5**, e14071 (2010). https://doi.org/10.1371/journal.pone.0014071

13 Duque, D., Pérez-González, D., Ayala, Y. A., Palmer, A. R. & Malmierca, M. S. Topographic distribution, frequency, and intensity dependence of stimulus-specific adaptation in the inferior colliculus of the rat. *J Neurosci* **32**, 17762-17774 (2012). https://doi.org/10.1523/jneurosci.3190-12.2012

14 Malmierca, M. S. & Auksztulewicz, R. Stimulus-specific adaptation, MMN and predictive coding. *Hear Res* **399**, 108076 (2021). https://doi.org/10.1016/j.heares.2020.108076

15 Lao-Rodríguez, A. B. *et al.* Neuronal responses to omitted tones in the auditory brain: A neuronal correlate for predictive coding. *Sci Adv* **9**, eabq8657 (2023). https://doi.org/10.1126/sciadv.abq8657

16 Zhai, Y. Y., Sun, Z. H., Gong, Y. M., Tang, Y. & **Yu*, X.** Integrative stimulus-specific adaptation of the natural sounds in the auditory cortex of the awake rat. *Brain Struct Funct* **224**, 1753-1766

(2019). https://doi.org/10.1007/s00429-019-01880-2

17 Zhai, Y. Y. *et al.* Synaptic Adaptation Contributes to Stimulus-specific Adaptation in the Thalamic Reticular Nucleus. *Neurosci Bull* **224**, 1753-1766 (2020). https://doi.org/10.1007/s00429-019-01880-2

18 Song, P., Zhai, Y. & **Yu*, X.** Stimulus-specific adaptation (SSA) in the auditory system: Functional relevance and underlying mechanisms. *Neurosci Biobehav Rev* **149**, 105190 (2023). https://doi.org/10.1016/j.neubiorev.2023.105190

19 Rui, Y. Y., He, J., Zhai, Y. Y., Sun, Z. H. & **Yu*, X.** Frequency-Dependent Stimulus-Specific Adaptation and Regularity Sensitivity in the Rat Auditory Thalamus. *Neuroscience* **392**, 13-24 (2018). https://doi.org/10.1016/j.neuroscience.2018.09.015

20 Gong, Y. *et al.* Cross-Modal Interaction and Integration Through Stimulus-Specific Adaptation in the Thalamic Reticular Nucleus of Rats. *Neurosci Bull* (2022). https://doi.org/10.1007/s12264-022-00827-8

21 Bussey, T. Novelty in the brain. *Trends in Cognitive Sciences* **3**, 126 (1999). https://doi.org/10.1016/S1364-6613(99)01305-4

22 Fitzgerald, K. & Todd, J. Making Sense of Mismatch Negativity. *Front Psychiatry* **11**, 468 (2020). https://doi.org/10.3389/fpsyt.2020.00468

23 Tiitinen, H., May, P., Reinikainen, K. & Näätänen, R. Attentive novelty detection in humans is governed by pre-attentive sensory memory. *Nature* **372**, 90-92 (1994). https://doi.org/10.1038/372090a0

24 Nelken, I. & Ulanovsky, N. Mismatch Negativity and Stimulus-Specific Adaptation in Animal Models. *Journal of Psychophysiology* **21**, 214-223 (2007). https://doi.org/10.1027/0269-8803.21.34.214

25 Fishman, Y. I. & Steinschneider, M. Searching for the Mismatch Negativity in Primary Auditory Cortex of the Awake Monkey: Deviance Detection or Stimulus Specific Adaptation? *Journal of Neuroscience* **32**, 15747-15758 (2012).

26 Taaseh, N., Yaron, A. & Nelken, I. Stimulus-specific adaptation and deviance detection in the rat auditory cortex. *PloS One* **6**, e23369 (2011). https://doi.org/10.1371/journal.pone.0023369

27 Grimm, S., Escera, C. & Nelken, I. Early indices of deviance detection in humans and animal models. *Biol Psychol* **116**, 23-27 (2016). https://doi.org/10.1016/j.biopsycho.2015.11.017

28 Yaron, A., Jankowski, M. M., Badrieh, R. & Nelken, I. Stimulus-specific adaptation to behaviorally-relevant sounds in awake rats. *PLoS One* **15**, e0221541 (2020). https://doi.org/10.1371/journal.pone.0221541

29 Shiramatsu, T. I. & Takahashi, H. Mismatch-negativity (MMN) in animal models: Homology of human MMN? *Hear Res* **399**, 107936 (2021). https://doi.org/10.1016/j.heares.2020.107936

30 Farley, B. J., Quirk, M. C., Doherty, J. J. & Christian, E. P. Stimulus-specific adaptation in auditory cortex is an NMDA-independent process distinct from the sensory novelty encoded by the mismatch negativity. *J Neurosci* **30**, 16475-16484 (2010). https://doi.org/10.1523/jneurosci.2793-10.2010

31 Erlbeck, H., Kübler, A., Kotchoubey, B. & Veser, S. Task instructions modulate the attentional mode affecting the auditory MMN and the semantic N400. *Frontiers in Human Neuroscience* **Volume 8 - 2014** (2014). https://doi.org/10.3389/fnhum.2014.00654

32 Du, X. *et al.* The multifaceted role of the inferior colliculus in sensory prediction, reward

processing, and decision-making. *Elife* **13** (2025). https://doi.org/10.7554/eLife.101142

33 Gong, Y. *et al.* Neural correlates of novelty detection in the primary auditory cortex of behaving monkeys. *Cell Rep* **43**, 113864 (2024). https://doi.org/10.1016/j.celrep.2024.113864

34 Du, X. *et al.* Protocol for behavioral and neural recording in macaques during a novelty detection task. *STAR Protoc* **5**, 103252 (2024). https://doi.org/10.1016/j.xpro.2024.103252

35 Parras, G. G. *et al.* Neurons along the auditory pathway exhibit a hierarchical organization of prediction error. *Nature Communications* **8**, 2148 (2017). https://doi.org/10.1038/s41467-017-02038-6

36 Carbajal, G. V. & Malmierca, M. S. The Neuronal Basis of Predictive Coding Along the Auditory Pathway: From the Subcortical Roots to Cortical Deviance Detection. *Trends Hear* **22**, 2331216518784822 (2018). https://doi.org/10.1177/2331216518784822

37 Heilbron, M. & Chait, M. Great Expectations: Is there Evidence for Predictive Coding in Auditory Cortex? *Neuroscience* **389**, 54-73 (2018). https://doi.org/10.1016/j.neuroscience.2017.07.061

38 Nieto-Diego, J. & Malmierca, M. S. Topographic Distribution of Stimulus-Specific Adaptation across Auditory Cortical Fields in the Anesthetized Rat. *PLOS Biology* **14**, e1002397 (2016). https://doi.org/10.1371/journal.pbio.1002397

39 Chao, Z. C., Huang, Y. T. & Wu, C. T. A quantitative model reveals a frequency ordering of prediction and prediction-error signals in the human brain. *Commun Biol* **5**, 1076 (2022). https://doi.org/10.1038/s42003-022-04049-6

40 Caucheteux, C., Gramfort, A. & King, J.-R. Evidence of a predictive coding hierarchy in the human brain listening to speech. *Nature Human Behaviour* **7**, 430-441 (2023). https://doi.org/10.1038/s41562-022-01516-2

41 Strube, A., Rose, M., Fazeli, S. & Büchel, C. Alpha-to-beta- and gamma-band activity reflect predictive coding in affective visual processing. *Scientific Reports* **11**, 23492 (2021). https://doi.org/10.1038/s41598-021-02939-z

42 Barron, H. C., Auksztulewicz, R. & Friston, K. Prediction and memory: A predictive coding account. *Prog Neurobiol* **192**, 101821 (2020). https://doi.org/10.1016/j.pneurobio.2020.101821

43 Plakke, B. & Romanski, L. M. Auditory connections and functions of prefrontal cortex. *Frontiers in Neuroscience* **Volume 8 - 2014** (2014). https://doi.org/10.3389/fnins.2014.00199

44 Nourski, K. V. *et al.* Cortical responses to auditory novelty across task conditions: An intracranial electrophysiology study. *Hearing Research* **399**, 107911 (2021). https://doi.org/https://doi.org/10.1016/j.heares.2020.107911

45 Cornella, M., Leung, S., Grimm, S. & Escera, C. Detection of Simple and Pattern Regularity Violations Occurs at Different Levels of the Auditory Hierarchy. *PLOS ONE* **7**, e43604 (2012). https://doi.org/10.1371/journal.pone.0043604

46 Chao, Z. C., Huang, Y. T. & Wu, C.-T. A quantitative model reveals a frequency ordering of prediction and prediction-error signals in the human brain. *Commun Biol* **5**, 1076 (2022). https://doi.org/10.1038/s42003-022-04049-6

47 Dhamala, M., Rangarajan, G. & Ding, M. Analyzing information flow in brain networks with nonparametric Granger causality. *NeuroImage* **41**, 354-362 (2008). https://doi.org/https://doi.org/10.1016/j.neuroimage.2008.02.020

48 Bressler, S. L. & Seth, A. K. Wiener–Granger Causality: A well established methodology. *NeuroImage* **58**, 323-329 (2011). https://doi.org/https://doi.org/10.1016/j.neuroimage.2010.02.059

49 Bastos, André M. *et al.* Visual Areas Exert Feedforward and Feedback Influences through Distinct Frequency Channels. *Neuron* **85**, 390-401 (2015). https://doi.org/10.1016/j.neuron.2014.12.018

50 Auksztulewicz, R. & Friston, K. Repetition suppression and its contextual determinants in predictive coding. *Cortex* **80**, 125-140 (2016). https://doi.org/10.1016/j.cortex.2015.11.024

51 Yu, X. J., Xu, X. X., He, S. & He, J. Change detection by thalamic reticular neurons. *Nature Neuroscience* **12**, 1165-1170 (2009). https://doi.org/10.1038/nn.2373

52 Chen, C., Xu, S., Wang, Y. & Wang, X. Location-specific neural facilitation in marmoset auditory cortex. *Nat Commun* **16**, 2773 (2025). https://doi.org/10.1038/s41467-025-58034-8

53 Gill, N. K. & Francis, N. A. Repetition plasticity in primary auditory cortex occurs across long timescales for spectrotemporally randomized pure-tones. *bioRxiv* (2023). https://doi.org/10.1101/2023.04.26.538446

54 Burke, R. *et al.* The role of delta phase for temporal predictions investigated with bilateral parietal tACS. *Brain Stimul* **18**, 103-113 (2025). https://doi.org/10.1016/j.brs.2024.12.1476

55 Majerus, S. *et al.* Cross-Modal Decoding of Neural Patterns Associated with Working Memory: Evidence for Attention-Based Accounts of Working Memory. *Cereb Cortex* **26**, 166-179 (2016). https://doi.org/10.1093/cercor/bhu189

56 Osmanski, M. S. & Wang, X. Behavioral dependence of auditory cortical responses. *Brain Topogr* **28**, 365-378 (2015). https://doi.org/10.1007/s10548-015-0428-4

57 Manea, A. M. G. *et al.* Neural timescales reflect behavioral demands in freely moving rhesus macaques. *Nat Commun* **15**, 2151 (2024). https://doi.org/10.1038/s41467-024-46488-1

58 Vinck, M., Uran, C., Dowdall, J. R., Rummell, B. & Canales-Johnson, A. Large-scale interactions in predictive processing: oscillatory versus transient dynamics. *Trends Cogn Sci* **29**, 133-148 (2025). https://doi.org/10.1016/j.tics.2024.09.013

59 Feldman, H. & Friston, K. J. Attention, uncertainty, and free-energy. *Front Hum Neurosci* **4**, 215 (2010). https://doi.org/10.3389/fnhum.2010.00215

60 Arnal, L. H. & Giraud, A. L. Cortical oscillations and sensory predictions. *Trends Cogn Sci* **16**, 390-398 (2012). https://doi.org/10.1016/j.tics.2012.05.003

61 Wilsch, A., Henry, M. J., Herrmann, B., Maess, B. & Obleser, J. Slow-delta phase concentration marks improved temporal expectations based on the passage of time. *Psychophysiology* **52**, 910-918 (2015). https://doi.org/10.1111/psyp.12413

62 Salimi, M., Tabasi, F., Nazari, M., Ghazvineh, S. & Raoufy, M. R. The olfactory bulb coordinates the ventral hippocampus-medial prefrontal cortex circuit during spatial working memory performance. *J Physiol Sci* **72**, 9 (2022). https://doi.org/10.1186/s12576-022-00833-5

63 Chao, Z. C., Takaura, K., Wang, L., Fujii, N. & Dehaene, S. Large-Scale Cortical Networks for Hierarchical Prediction and Prediction Error in the Primate Brain. *Neuron* **100**, 1252-1266 e1253 (2018). https://doi.org/10.1016/j.neuron.2018.10.004

64 Durschmid, S. *et al.* Hierarchy of prediction errors for auditory events in human temporal and frontal cortex. *Proc Natl Acad Sci U S A* **113**, 6755-6760 (2016). https://doi.org/10.1073/pnas.1525030113

65 Camalier, C. R., Scarim, K., Mishkin, M. & Averbeck, B. B. A Comparison of Auditory Oddball

Responses in Dorsolateral Prefrontal Cortex, Basolateral Amygdala, and Auditory Cortex of Macaque. *J Cogn Neurosci* **31**, 1054-1064 (2019). https://doi.org/10.1162/jocn_a_01387

66 Feldman, H. & Friston, K. Attention, Uncertainty, and Free-Energy. *Frontiers in Human Neuroscience* **Volume 4 - 2010** (2010). https://doi.org/10.3389/fnhum.2010.00215

67 Song, P. *et al.* Temporal merging into pitch with click train in the macaque auditory cortex. *National Science Review* (2025). https://doi.org/10.1093/nsr/nwaf026

68 Gong, Y. *et al.* Neural correlates of novelty detection in the primary auditory cortex of behaving monkeys. *Cell Reports* **43**, 113864 (2024). https://doi.org/https://doi.org/10.1016/j.celrep.2024.113864

69 Oostenveld, R., Fries, P., Maris, E. & Schoffelen, J. M. FieldTrip: Open source software for advanced analysis of MEG, EEG, and invasive electrophysiological data. *Comput Intell Neurosci* **2011**, 156869 (2011). https://doi.org/10.1155/2011/156869

70 Rouder, J. N., Speckman, P. L., Sun, D., Morey, R. D. & Iverson, G. Bayesian t tests for accepting and rejecting the null hypothesis. *Psychonomic Bulletin & Review* **16**, 225-237 (2009). https://doi.org/10.3758/PBR.16.2.225

71 Rouder, J. N., Morey, R. D., Speckman, P. L. & Province, J. M. Default Bayes factors for ANOVA designs. *Journal of Mathematical Psychology* **56**, 356-374 (2012). https://doi.org/https://doi.org/10.1016/j.jmp.2012.08.001

72 klabhub/bayesFactor: Bayes only v. v3.0 (Zenodo, 2024).